SANDIA REPORT

SAND2004-0567
Unlimited Release
Printed February 2004

Mesoscale Wide-Bandwidth Linear Magnetic Actuators: An LDRD Final Report

Lawrence A. Jones

Prepared by
Sandia National Laboratories
Albuquerque, New Mexico 87185 and Livermore, California 94550

Sandia is a multiprogram laboratory operated by Sandia Corporation,
a Lockheed Martin Company, for the United States Department of Energy's
National Nuclear Security Administration under Contract DE-AC04-94AL85000.

Issued by Sandia National Laboratories, operated for the United States Department of Energy by Sandia Corporation.

Available to DOE and DOE contractors from
U.S. Department of Energy
Office of Scientific and Technical Information
P.O. Box 62
Oak Ridge, TN 37831

Telephone: (865)576-8401
Facsimile: (865)576-5728
E-Mail: reports@adonis.osti.gov
Online ordering: http://www.doe.gov/bridge

Available to the public from
U.S. Department of Commerce
National Technical Information Service
5285 Port Royal Rd
Springfield, VA 22161

Telephone: (800)553-6847
Facsimile: (703)605-6900
E-Mail: orders@ntis.fedworld.gov
Online order: http://www.ntis.gov/help/ordermethods.asp?loc=7-4-0#online

SAND2004-0567
Unlimited Release
Printed February 2004

Mesoscale Wide-Bandwidth Linear Magnetic Actuators: An LDRD Final Report

Lawrence A. Jones
Electronic Systems Center
Sandia National Laboratories
P.O. Box 5800
Albuquerque, NM 87185–0501

Abstract

As MEMS transducers are scaled up in size, the threshold is quickly crossed to where magnetoquasistatic (MQS) transducers are superior for force production compared to electroquasistatic (EQS) transducers. Considerable progress has been made increasing the force output of MEMS EQS transducers, but progress with MEMS MQS transducers has been more modest. A key reason for this has been the difficulty implementing efficient lithographically-fabricated magnetic coil structures.

The contribution of this study is a planar multilayer polyphase coil architecture which provides for the lithographic implementation of efficient stator windings suitable for linear magnetic machines. A millimeter-scale linear actuator with complex stator windings was fabricated using this architecture.

The stators of the actuator were fabricated using a BCB/Cu process, which does not require replanarization of the wafer between layers. The prototype stator was limited to thin copper layers (3 μm) due to the use of evaporated metal at the time of fabrication. Two layers of metal were implemented in the prototype, but the winding architecture naturally supports additional metal layer pairs.

It was found in laboratory tests that the windings can support very high current densities of $4 \times 10^9 \mathrm{A/m}^2$ without damage. Force production normal to the stator was calculated to be 0.54 N/A. For thin stators such as this one, force production increases approximately linearly with the thickness of the windings and a six-layer stator fabricated using a newly implemented electroplated BCB/Cu process (six layers of 15 μm thick metal) is projected to produce approximately 8.8 N/A.

Acknowledgments

The author wishes to thank the following individuals for their contributions:

- Rajen Chanchani (1745) for overseeing the implementation of the BCB/Cu HDI process at Sandia and the lithographic fabrication of the stator windings in this project.
- Denise B. Webb (1745) for fabricating the wafers.
- Donald Bethke (1745) for assisting with the wafer processing.
- Cynthia D. Blain (2339) for soldering leads on to the wafer.
- Michael P. Saavedra (14184) for cutting the permanent magnets on the micro-EDM machine.
- Thomas K. Mayer (15252) for designing and fabricating the actuator test stand.

Contents

1 Introduction **7**

2 Literature Review **11**

3 Actuator Architecture **13**

4 Fabrication Process **20**

5 Results **21**

6 Conclusions **23**

7 Future Work **24**

A Actuator Parameters **26**

B Platen **28**

C Wafer Design **33**

D Force Modeling **41**

E Dynamics **43**

F Control **46**

G Force Allocation **49**

H Commutation **51**

I Measurements **53**

List of Figures

1 Maximum energy densities in MQS and EQS MEMS systems 8
2 Maximum energy densities at fixed voltages in EQS MEMS systems . . . 9
3 Macroscale magnetically-levitated planar actuator 10
4 Lithographically-fabricated linear motor stators on a wafer 13
5 Wafer mask drawing 14
6 Armature magnet arrays embedded in the platen 15
7 Mesoscale magnetically-levitated planar actuator 16
8 Single coil construction 17
9 Polyphase planar winding 18
10 Polyphase planar winding with pole-to-pole connections 19
11 Current flow in multiple layer-pair stators 20
12 Conductor dimensions in the prototype actuator 22
13 Halbach magnet arrays mounted in the platen 28
14 Halbach magnet array fabrication drawing 29
15 Platen fabrication drawing 31
16 Halbach magnet array flux density 32
17 Mask for metal layer 1 34
18 Mask for metal layer 2 35
19 Mask for metal layer 3 36
20 Mask for metal layer 4 37
21 Mask for metal layer 5 38
22 Mask for metal layer 6 39
23 Wafer detail photograph 40
24 Example wafer defects 40
25 Vertical servo model loop transmission 47
26 Vertical servo model closed-loop response 47
27 Vertical servo model step response 48
28 Lateral positions of the magnet arrays in the platen 50
29 Platen constrained to vertical motions 53
30 Measured vertical servo staircase response 54
31 Measured vertical servo step response 55

1 Introduction

Electroquasistatic (EQS) transducers are commonly used in micro-electromechanical systems (MEMS), ostensibly because the fabrication of electrode plates in EQS transducers is relatively simple and is compatible with the materials and processes of silicon microfabrication technology. Elaborate comb structures with hundreds of electrodes have been fabricated to increase the force produced by EQS transducers [1]. While EQS transducers are electrically more efficient than magnetoquasistatic (MQS) transducers at all speeds [2], MQS transducers can generate more force than EQS transducers at all but the smallest sizes.

The force generated by a transducer is equal to the negative spatial gradient of the energy W in the air gap between the armature and the stator,[1]

$$f = -\nabla W \,. \tag{1}$$

Maximizing the energy W in the air gap will maximize the generated force. Equivalently, maximizing the energy density w in the air gap will maximize the generated force. In a linear MQS system, the energy density in the air gap is

$$w_m = \frac{B^2}{2\mu_o} \tag{2}$$

and in a linear EQS system, the energy density in the air gap is

$$w_e = \frac{\epsilon_o E^2}{2} \,. \tag{3}$$

If the electric field in the air gap is uniform and normal to the electrodes, then $E = V/g$, where V is the potential difference between the electrodes and g is the distance between the electrodes. Hence,

$$w_e = \frac{\epsilon_o V^2}{2g^2} \,. \tag{4}$$

In MQS systems, the maximum flux density B is often limited by saturation of the high-permeability materials in the flux paths because generating higher flux densities may require prohibitively greater amounts of magnetomotive force. Saturation in high-permeability irons typically occurs around 1.5 T, and in nickel-iron systems at around 1 T [4]. Flux path saturation is independent of the size g of the air gap.

[1]The force generated is equal to the negative spatial gradient of the energy W when flux linkage and charge are taken to be the independent variables in MQS and EQS systems, respectively. Currents and voltages are then dependent variables described by the terminal relations

$$i = i(\lambda, x), \qquad v = v(q, x) \,.$$

If currents and voltages are the independent variables, then the coenergy W' must be used to compute the force [3]. In electrically linear systems, energy and coenergy are numerically equal.

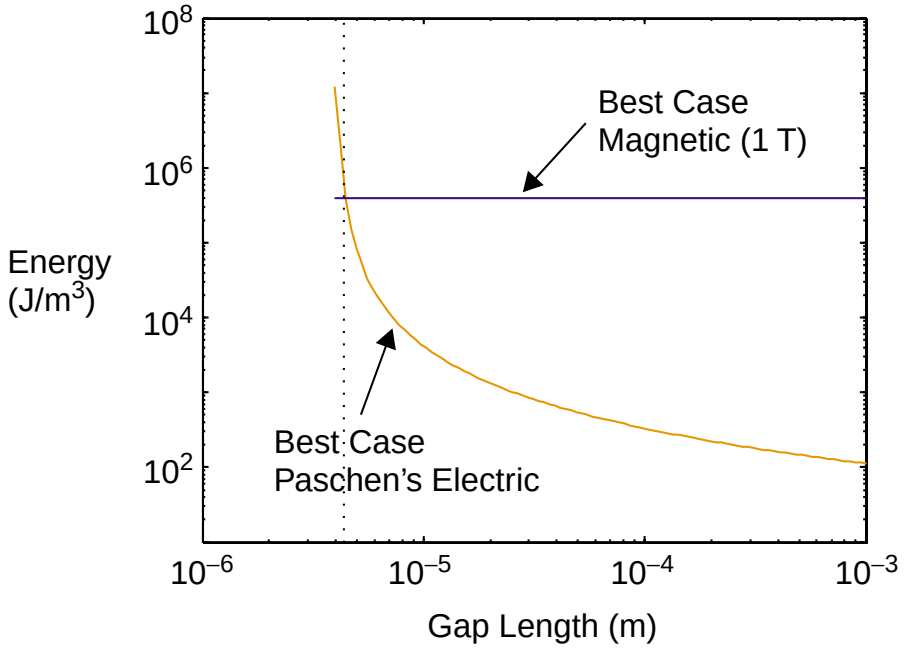

Figure 1: Maximum energy densities achievable in MQS and EQS MEMS systems [7].

In EQS systems, the maximum energy density is limited by voltage breakdown in the air gap between the electrodes. As the separation between the electrodes decreases below 10 μm at constant atmospheric pressure, the breakdown voltage *increases* according to Paschen's curve [5, 6]. Substituting the breakdown voltages of Paschen's curve into (4) yields the maximum EQS energy density curve shown in Figure 1.

The maximum MQS energy density is significantly greater than the maximum EQS energy density at all but the smallest air gap sizes. It should be noted that when there are imperfections on the electrodes, the breakdown voltages on Paschen's curve cannot be achieved, and hence the maximum EQS energy density shown in Figure 1 is a hard upper bound in one atmosphere. (The EQS voltage at the crossover point in Figure 1 is approximately 1500 V.) When the voltages used to drive EQS MEMS device are limited to values typically found in integrated circuits, the achievable energy densities are even more modest, as shown in Figure 2.

In contrast, the MQS maximum shown is fixed only by saturation in the flux path. With sufficient magnetomotive force, the air gap can support up to two orders of magnitude greater flux density [8] and hence, by (2), four orders of magnitude greater energy density. High-energy permanent magnets are magnetomotive sources that scale well to small sizes. Permanent magnet energy densities continue to improve each year, and a breakthrough in room-temperature superconductors could substantially raise the MQS

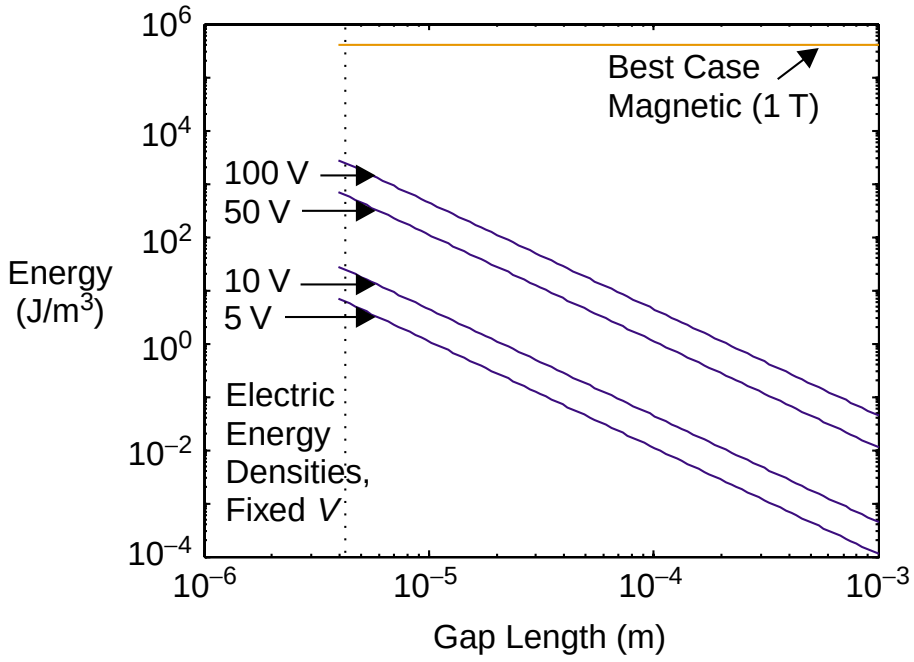

Figure 2: Maximum energy densities at fixed voltages in EQS MEMS systems (adapted from [7]).

limit in Figures 1 and 2.

A conclusion from Figure 1 is that for all but the smallest air gaps, MQS systems are superior for force production. This observation explains why virtually all macroscale electric motors and generators utilize magnetic fields and not electric fields. As MEMS transducers are scaled up in size, the threshold is quickly crossed to where MQS transducers are superior—if they can be fabricated. In *mesoscale* systems, defined here as millimeter-scale systems, armature-stator air gaps of approximately 50 μm are achievable and Figure 1 shows that MQS systems are superior. Further arguments favoring MQS transducers over EQS transducers at all but the smallest size scales may be found in [8].[2] Some counter arguments in favor of EQS systems, largely based on the difficulty of fabricating MQS systems, are given in [7]. A key feature of MQS transducers for applications identified in the present study is their inherent low impedance, making them resistant to upset by charge-inducing events.

In the present study, improved ways were sought to efficiently fabricate complex magnetic windings for somewhat larger—mesoscale—actuators. A linear mesoscale actuator

[2]Although the case is argued for MQS actuators in [8], a more general indictment is made of the whole concept of microfabricated actuators. Although published more than ten years ago, most of the indictments are surprisingly valid today.

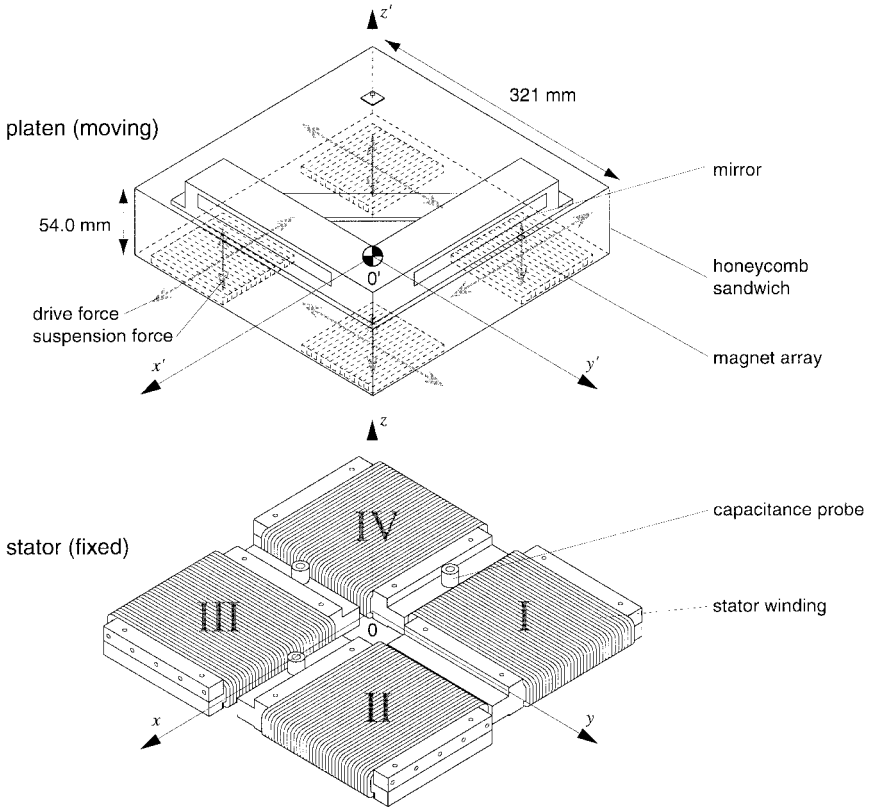

Figure 3: The macroscale magnetically-levitate planar actuator that was implemented in [9]. Four wire-wound stators and four facing permanent magnet armatures formed two motors in x and z and two motors in y and z.

was developed where the fabrication of polyphase windings using conventional wire would be very difficult. At the same time, the size of the actuator was kept large enough that high-energy sintered permanent magnet materials could be magnetized first and then assembled into the actuator without undue difficulty. The throw range of the actuator was chosen to be well beyond the throw range of piezoelectric stacks.

Numerous mesoscale linear magnetic actuator concepts, both original and in the literature, were considered where the windings might be fabricated using MEMS processes. The macroscale, magnetically-levitated, planar actuator in [9] was identified as being particularly well suited for miniaturization using MEMS-fabricated windings due to its mechanical simplicity and precision requirements. This macroscale actuator is shown in Figure 3. A platen containing four permanent magnet armatures is magnetically levitated over four planar stators. The four motors both levitate and propel the platen laterally in two dimensions. The design contains no high-permeability materials that might cause problematic trapping and cogging forces. As such, the actuator is optimized for high

precision rather than high force. The magnetic bearing conveniently avoids the friction problems that arise in MEMS devices but at the expense of higher power dissipation in the stator windings.

The high-performance operation of this actuator depends partly on the smoothness of the surface of the stator windings. Achieving a smooth stator surface becomes more difficult as the overall size of the actuator is reduced.[3] A very smooth surface can be achieved if the stator windings are fabricated on a wafer using a lithographic process. Other benefits of a lithographic approach for this actuator include very accurate coil geometry definition, very accurate relative positioning of the stators, and the ability to batch fabricate the stators. If lithographically-fabricated stators could be made that have a high enough current-handling capability (possibly using a multi-layer LIGA process), a lithographic approach could even be used to fabricate the stators for macroscale actuators such as the one in [9]. A finding of the present study is that lithographically-fabricated stators appear to support significantly higher current densities than conventionally wound stators.

For the present study, a multilayer planar polyphase coil architecture was developed that can be fabricated with any number of lithographic MEMS processes. The architecture is based on split-level spiral coils that are uniquely suited for implementing windings in planar linear actuators. To demonstrate the new coil architecture, a prototype actuator approximately one-fifth the size of the actuator in [9] was fabricated using a lithographic high-density interconnect (HDI) process.

2 Literature Review

Considerable progress has been made increasing the force output of MEMS EQS transducers (see [1], for example). Progress implementing MEMS MQS transducers, on the other hand, has been more modest. The primary reasons for this are (a) the difficulty of implementing coil structures, (b) the need for high-permeability materials not typically found in integrated circuit fabrication processes, and (c) the difficulty of magnetizing high-energy permanent magnet materials in-place. The last issue has prevented the development of micron-scale transducers with high-energy permanent magnets. MEMS actuators utilizing high-energy permanent magnets have been millimeter-scale devices.

Early efforts to produce MEMS MQS transducers focused on variable-reluctance transducers where the coils were external to the structure of the actuator and were wound with conventional wire [10]. With such devices, it was learned how to micro-fabricate the high-permeability materials required for variable-reluctance transducers.

Fabricating high-permeability materials in-place is also of interest for fabricating MEMS inductors. The coil topologies required for inductors are relatively simple and

[3]Fabrication of a prototype stator, identical to the actuator in [9] but approximately one-fifth the size, was attempted using individual coils wound with 43 gauge wire. A commercial vendor that specializes in winding microcoils tried numerous time without success to wind coils that when assembled into a stator created a smooth stator surface.

progress has been made in lithographically fabricating inductor coils with high-permeability cores. The simplest lithographically-fabricated coil topology is a spiral on a single layer and a variety of implementations have been reported. Single-layer planar spiral coils were stacked in [11] and [12] to form inductors. An actuator was formed from an array of lithographically-fabricated single-layer spiral coils in [13]. The array of coils faced an array of small permanent magnets glued to the backside of a deformable mirror. A similar array of single-layer spiral coils was fabricated in [14] to attract and repel a facing rigid planar array of magnets.

Implementations of single-layer planar coils for rotary magnetic actuators are reported in [15] and [16]. In [15], two layers of spiral coils for an axial flux rotary actuator were azimuthally offset from each other on either side of a supporting foil. The rotor, approximately 12 mm in diameter, was made my injection molding bonded magnet material. In [16], six layers of spiral coils were built up lithographically, with each layer offset azimuthally. Rotors, 1.6 mm and 1.9 mm in diameter, for the axial flux motor in [16] were cut from bulk sintered high-energy permanent magnet material using electro-discharge machining. Up to twelve poles were then magnetized on the rotors. Impressive magnetic remanences of approximately 0.8 T were achieved.

More sophisticated fabrication efforts have attempted to spread coils across multiple layers. In [17], a conductor was spiraled around high-permeability material such that the magnetization vector of the coil was parallel to the fabrication plane. The goal was coils that drive flux through in-plane variable reluctance actuators, and hence represents the next evolutionary step from the earlier work in [10].

The coil architecture closest to the present study is reported in [18]. In [18], the stator coils for an axial flux rotary motor were fabricated across two layers such that each stator phase formed a continuous helix around the azimuthal axis of the stator. The conductors of each stator phase traveled continuously around the stator, contributing to each pole pitch in the phase. This seemingly innocuous change from single-layer spiral coils, as in [15] and [16], to continuous helical coils is significant in that the packing factor of the continuous split-level helical winding is much greater.

The architecture in [18] is unique to rotary machines and not suitable for linear machines. In a rotary machine, the conductors within a phase can travel continuously around the stator, contributing to each pole pitch. In a linear machine, the stator does not begin and end at the same place and hence each pole pitch in a phase needs to be self-contained in order to avoid numerous return conductors traveling from the end of the stator back to the beginning, as would be the case if the winding structure in [18] were used for a linear machine. In other words, spiral coils are needed like those in [15] and [16]. The problem with the single-layer spiral coils in [15] and [16] is that it is not possible to implement more than one phase per layer because the sides and end-turns of each coil form a closed polygon in the layer, excluding access to the middle of the coil.

The coil architecture in the present study yields a stator suitable for linear machines, but with a high packing factor as in [18]. Spiral coils are split across two layers: one half of a coil on an upper layer and the other half of the coil on a lower layer. Split-level

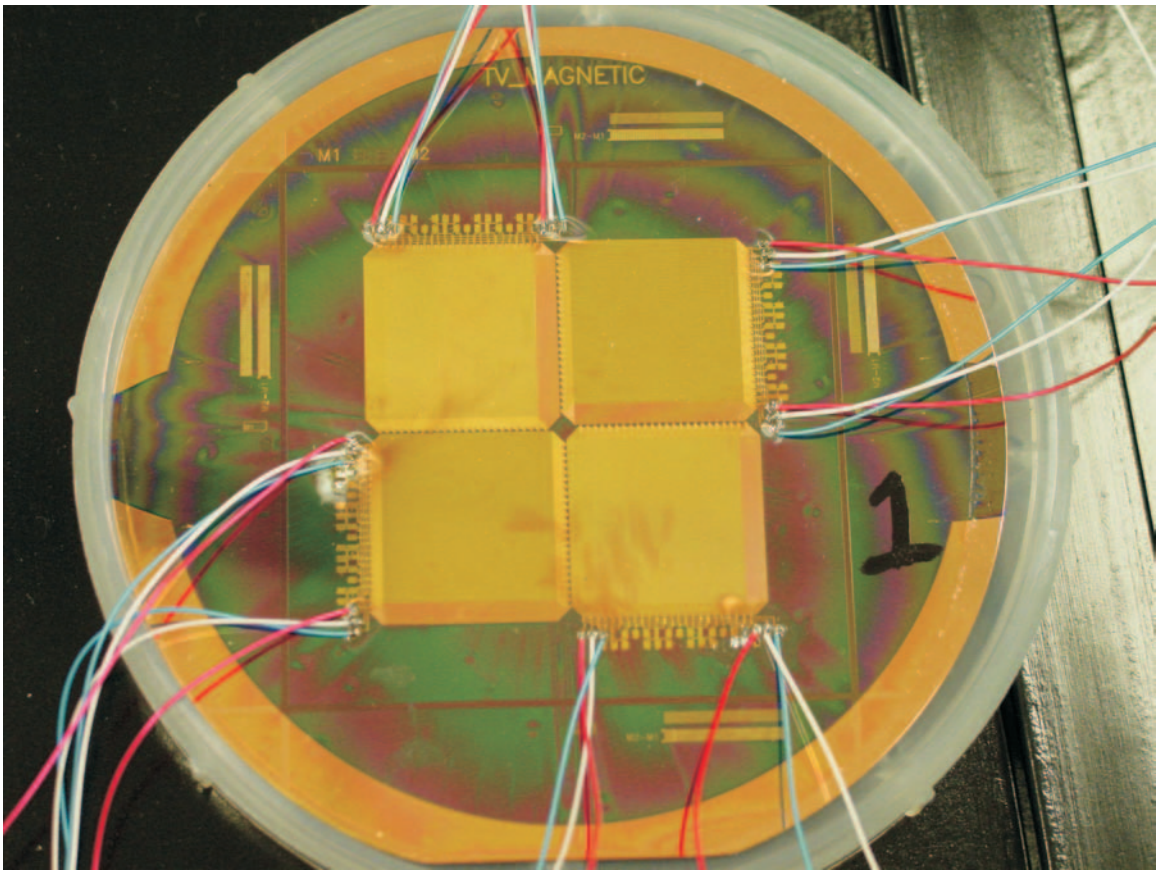

Figure 4: Four linear motor stators lithographically fabricated on a 4-inch silicon wafer.

spiral coils do not form a closed polygon on each layer, thereby allowing the middle of each coil to be filled with conductors from other phases.

3 Actuator Architecture

The actuator fabricated in the present study is conceptually identical to the actuator in [9]. The implementation differences are that the actuator here is approximately one-fifth the size and the stators were lithographically fabricated rather than assembled from individual wire coils. An example wafer with four lithographically-fabricated linear motor stators is shown in Figure 4. A mask drawing for the four-inch silicon wafer is shown in Figure 5.

The platen that faces the wafer is shown in Figure 6. The platen is levitated and translated over the wafer using the normal and tangential forces produced by the four embedded permanent magnet armatures interacting with the stators. Each armature is

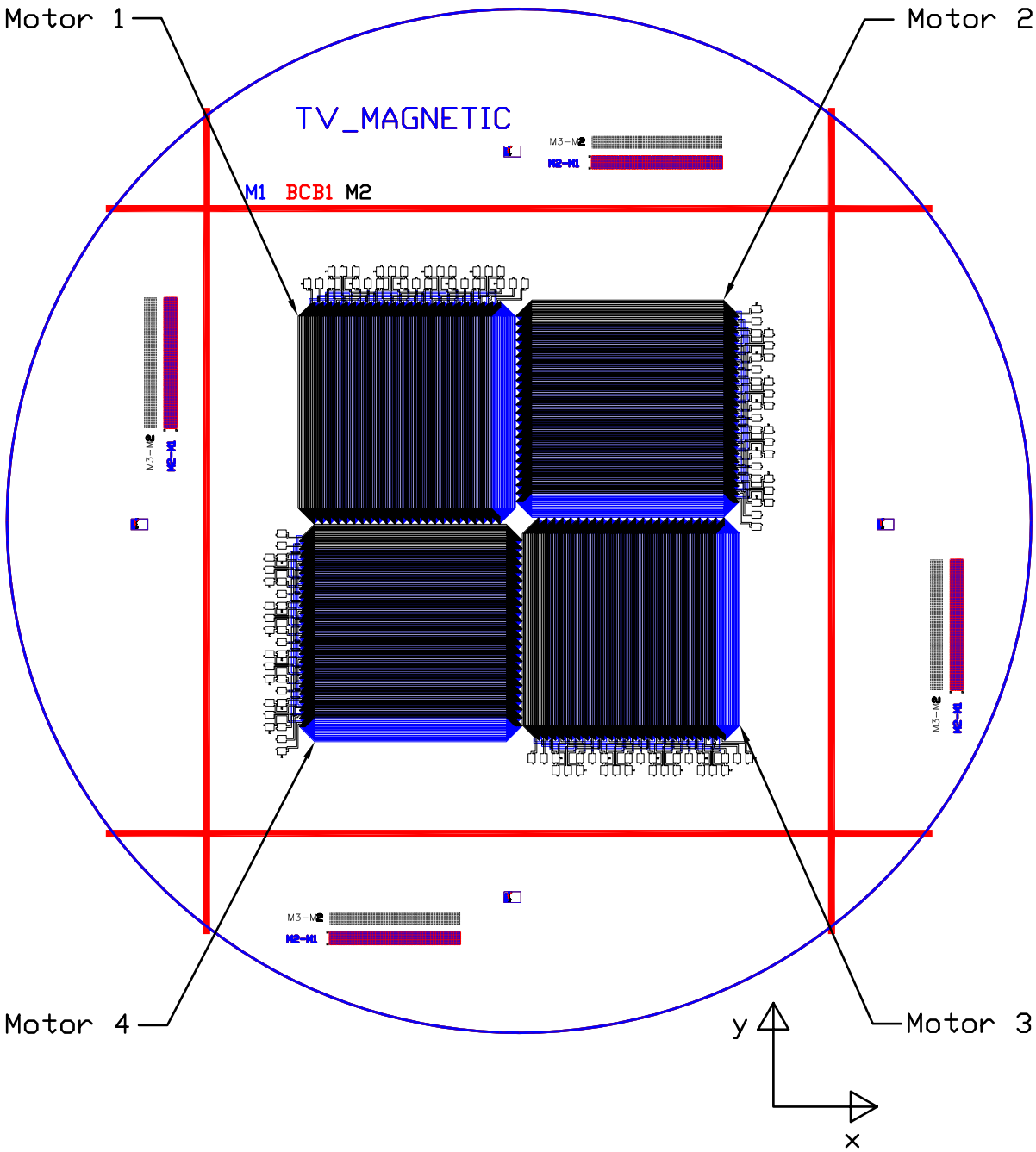

Figure 5: Wafer mask drawing with the four motor stators indicated. Motors 1 and 3 actuate in x and z (out of the page), while motors 2 and 4 actuate in y and z.

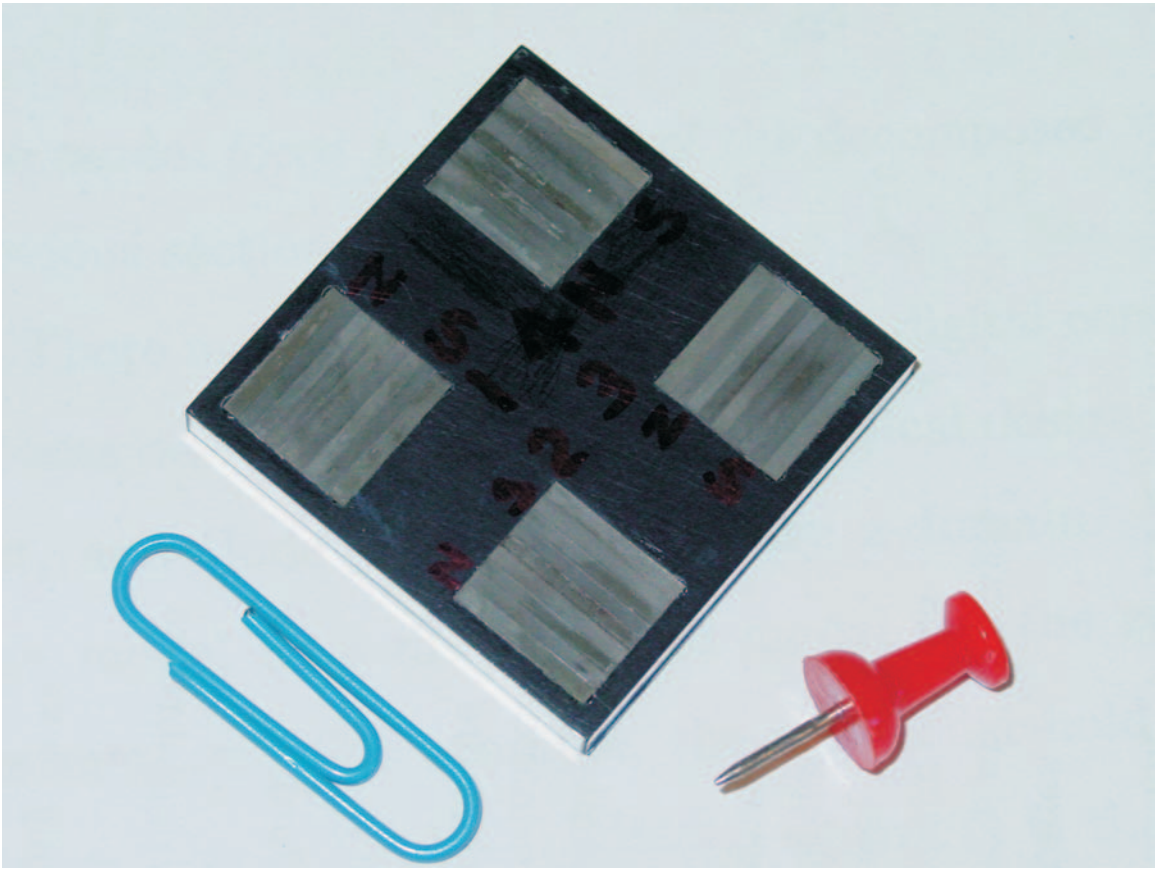

Figure 6: Platen surface facing the wafer. Four permanent magnet armatures are embedded in the platen surface facing the stators. Each armature is a nine-magnet Halbach array.

a nine-magnet Halbach array. The Halbach arrays exhibit at enhanced magnetic field on the side facing the stator windings and a reduced magnetic field on the away side. The platen and its magnet arrays are discussed further in Appendix B.

The platen and wafer are shown together in Figure 7. When the motors are operating, the platen is levitated and moved laterally over the wafer by the four motors. Closed-loop servoing of the platen is necessary because the lateral dynamic modes are unstable. Six laser displacement sensors are used to provide position feedback. The peak-to-peak throw of the actuator is 6 mm in both x and y.

Motors 1 and 3 in Figure 5 are oriented so that they can produce z-directed normal forces (out of the page) and x-directed tangential forces. Motors 2 and 4 are oriented so that they can produce z-directed normal forces and y-directed tangential forces. Figure 5 shows that Motor 3 is a mirror image of Motor 1 and Motor 4 is a mirror image of Motor 2.

As previously stated, the general topology of four motors levitating and translating

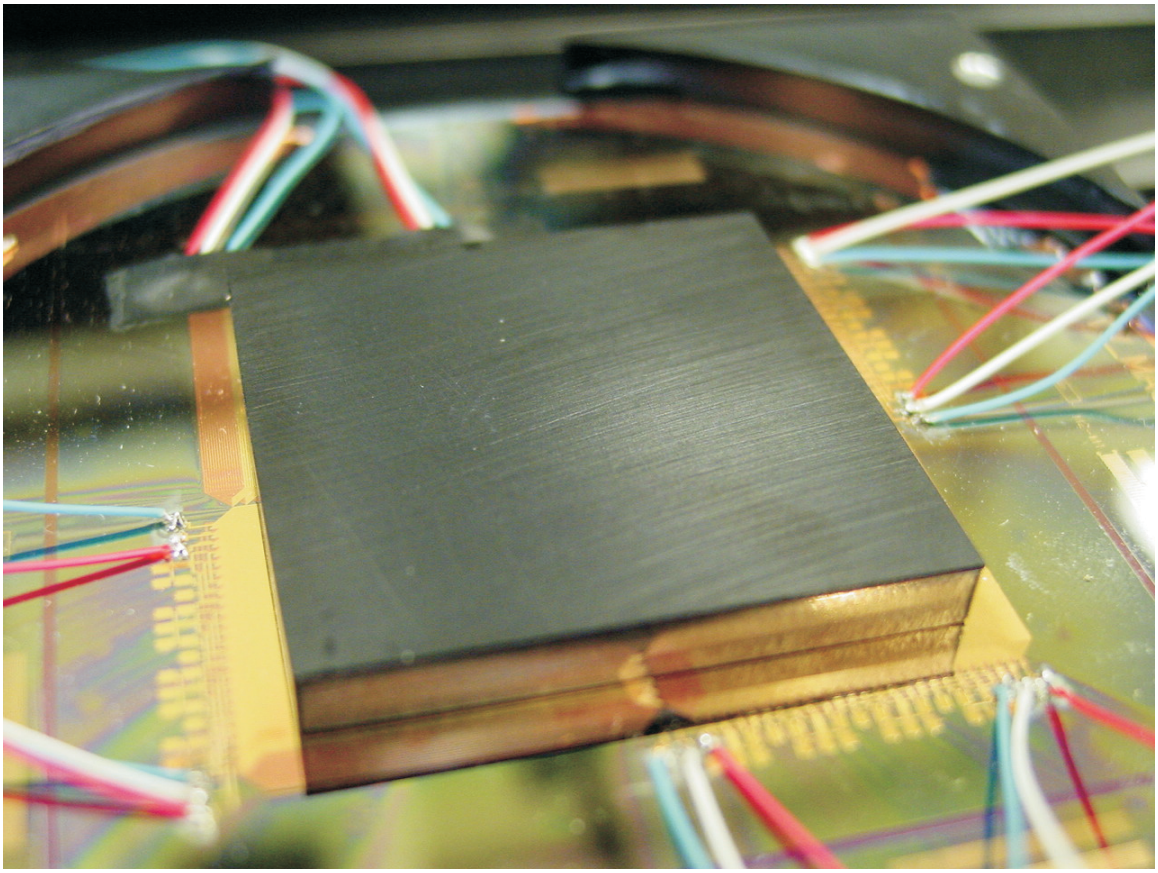

Figure 7: Mesoscale magnetically-levitated planar actuator with lithographically-fabricated stator windings. The platen is levitated and moved laterally over the wafer forming an x-y table.

a platen is not new. The novel aspects of the actuator in the this study are associated with the stator, its structure, and the process used to fabricate it. Therefore, the stator is examined in more detail next.

An illustration of a single coil of one phase of a stator is shown in Figure 8. The left side of the coil resides on an upper metal layer and the right side of the coil resides on a lower metal layer with vias connecting the two layers at the top and the bottom of the coil. The coil starts with a conductor on the top layer at the left edge and spirals inward, switching back and forth between the upper layer when it is on the left and the lower layer when it is on the right. As noted in Section 2, coils that are split between two layers are reported in [18]. However, the conductors in [18] traveled continuously from pitch to pitch around a circular stator forming a helical winding about the azimuthal axis of the stator. The conductors in Figure 8 form a self-contained split-level spiral coil for each pole pitch.

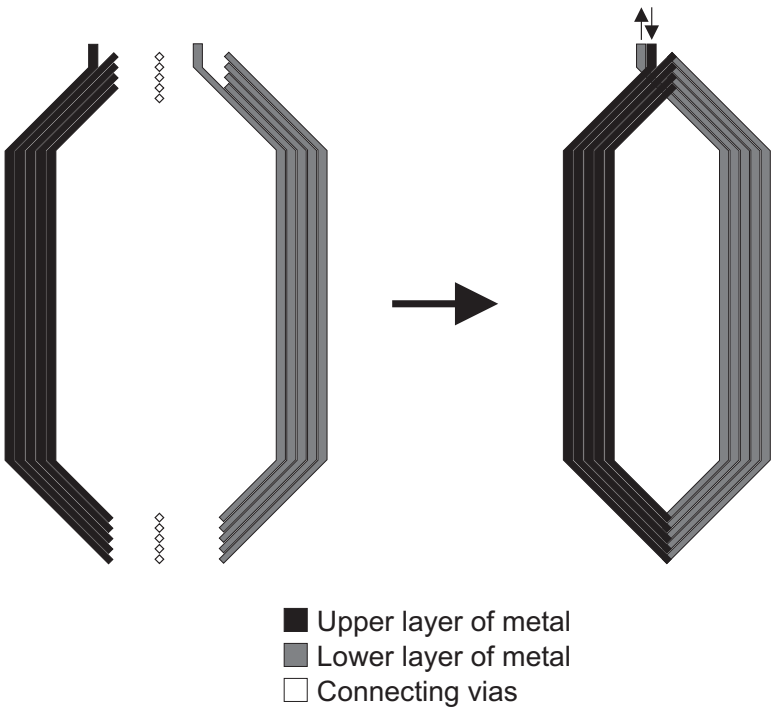

Figure 8: Illustration of the construction of a single coil of one phase of the stator. The conductors form a self-contained split-level spiral coil for each pole pitch. (Illustration not to scale).

Using these split-level coils, a polyphase planar winding with multiple pole pitches can be formed by overlapping the coils, as shown in Figure 9. Dark lines in Figure 9 indicate conductors on the upper layer and gray lines indicate conductors on the lower layer. The winding shown is a full-pitch winding and therefore the conductors of one pole pitch in a phase fully overlap the conductors of the next pole pitch in the phase. A fractional-pitch winding is possible with a similar coil structure. The winding in Figure 9 is a three-phase winding, but any number of phases is possible using the split-level coils. In the parlance of electric machinery windings, the architecture presented here is a prismatic implementation of a double-layer winding.

The multiple pole pitches of a phase are connected by conductors at one end of the coils, as shown in Figure 10. Figure 10 shows that the coils are connected such that the direction of current flow alternates with each pole pitch; in one pole pitch the current spirals counter-clockwise inward and in the next pole pitch it spirals clockwise outward. With these connections, current in overlapping conductors of adjacent pole pitches flows in the same direction.

Thus far only two layers of metal have been shown, but additional metal layer pairs that implement split-level coils can—and most likely should—be stacked to obtain a thicker stator. It was shown in [19] that the power optimal thickness of the stator wind-

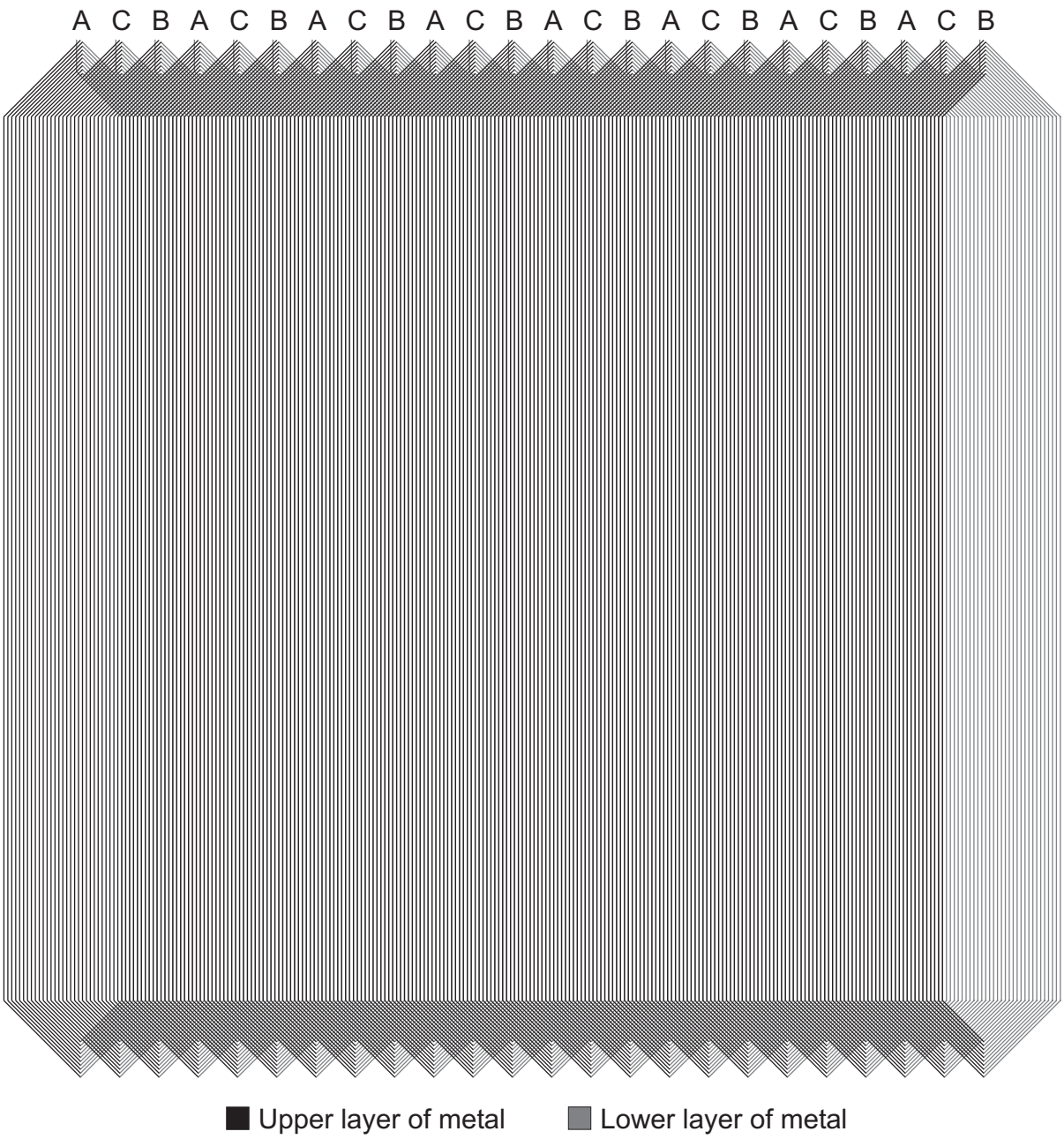

Figure 9: Polyphase planar winding formed by overlapping the split-level coils illustrated in Figure 8.

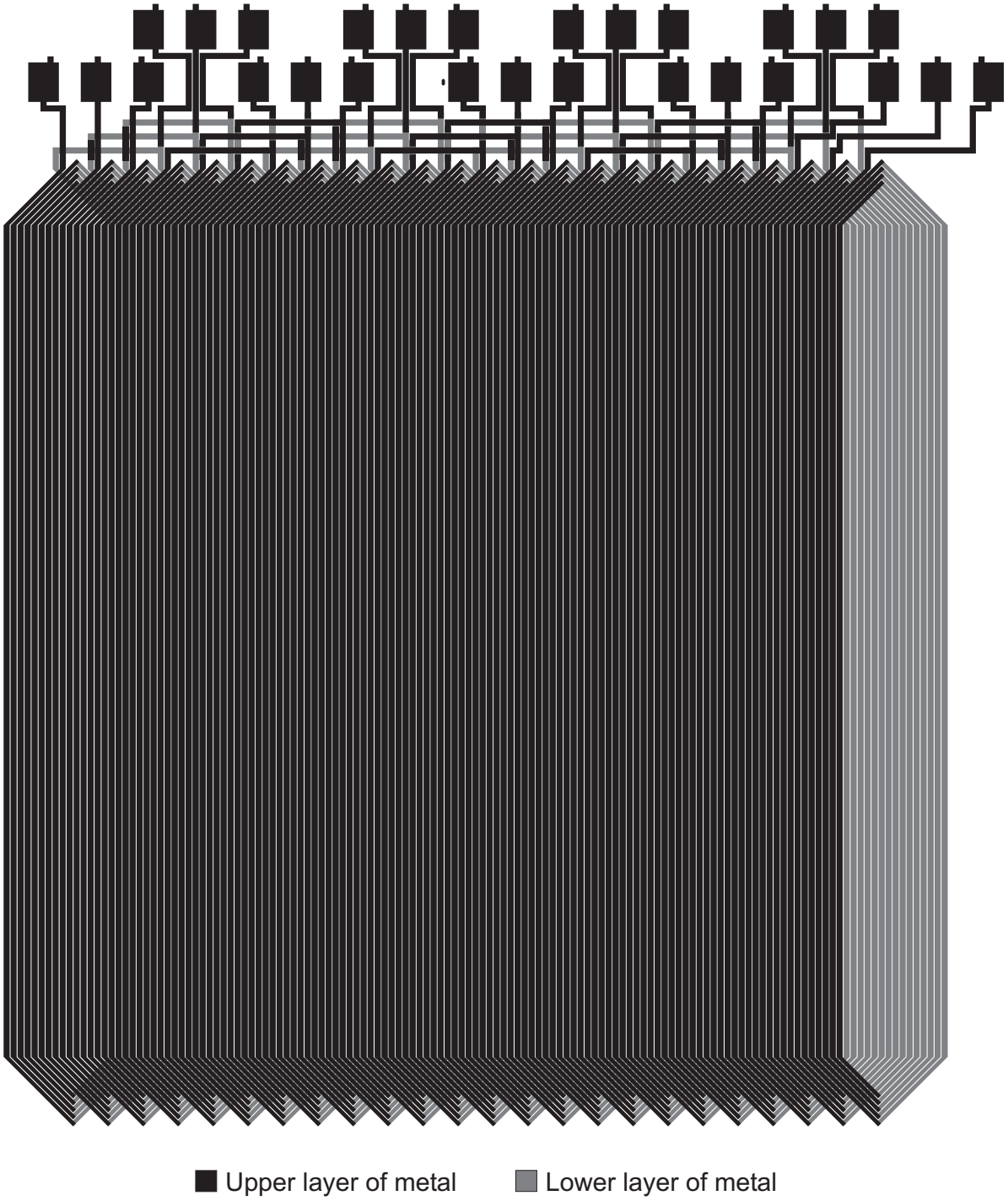

Figure 10: Double-layer polyphase planar winding with pole-pitch connections on one end. Pads for each pitch of each phase were brought out for testing purposes. The last set of pads on the far right can be connected together to form a three-phase Y connection.

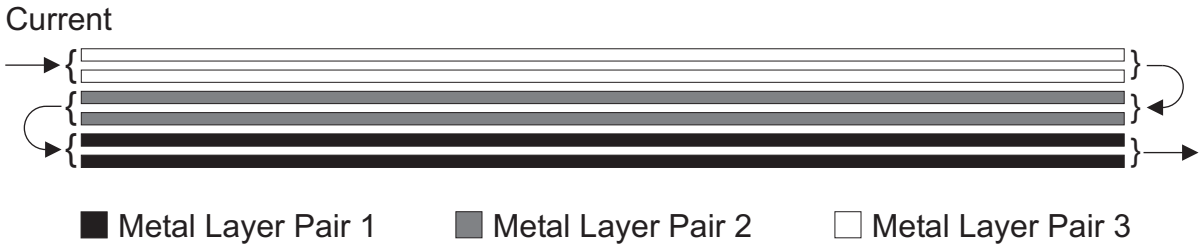

Figure 11: Current flow in multiple layer-pair stators. Metal layer pairs can be stacked to realize thicker stators. The current flow pattern illustrated allows each metal layer pair to be fabricated and tested before continuing with the fabrication of the next metal layer pair.

ings in a synchronous machine with Halbach arrays is one-fifth the fundamental spatial period of the magnetic field in the machine. The flow of current through multiple layer pairs is illustrated in Figure 11 for a six-layer stator. The particular current flow pattern shown was chosen to ease fabrication in that each metal layer pair can be fabricated and tested before continuing with the fabrication of the next metal layer pair.

4 Fabrication Process

The split-level spiral coil architecture described in Section 3 can support any number of phases, any amount of pitch overlap, and any number of turns in the pole pitches. The cross-section of the individual conductors in the coils, however, depends on the requirements of the application and the lithographic process used to fabricate the coils. Generally speaking, multiple turns in a stator coil are used to enforce a required current density throughout the volume of the coil. Multiple turns also increase the resistance of the coil, which makes it easier to control the current in the coil, albeit with greater power dissipation. The cross-section of each conductor and the number turns per coil is chosen to satisfy these (and possibly other) requirements.

The lithographic processes that might be used to fabricate multiple layers of patterned conductors and dielectric for the high-current stators in mesoscale actuators can be broken into two classes: lapped processes and non-lapped processes. In lapped processes, the dielectric layers used to construct a planar coil must be mechanically replanarized before continuing with the next layer of metal. An advantage of these processes is that each metal layer can be very thick, for example up to several hundred microns with LIGA processes. Thick metal patterns will create undulations in the next dielectric layer, making it non-planar. The dielectric layer is therefore planarized by mechanical lapping. The application of lapped processes is reported in [15, 16, 11, 18, 17].

In non-lapped processes, a liquid polymer dielectric is deposited on a metal pattern. The liquid polymer flows on the wafer surface and planarizes the undulations due to metal pattern before the polymer is cured. The self-replanarization of the liquid polymers is

not as complete as with mechanical lapping and hence the thickness of the metal layers is limited to several tens of microns. Nevertheless, the elimination of lapping substantially reduces the number of costly processing steps. The application of a non-lapped process is reported in [12]. A non-lapped process similar to that reported in [12] was used in the present study to fabricate the stator coils described in Section 3.

The benzocyclobutene/copper (BCB/Cu) high-density interconnect (HDI) process was used to fabricate the stators. The dielectric benzocyclobutene is a Dow Chemical Company trade mark product from the cyclotene family. The detailed properties of this family of polymers may be found at www.cyclotene.com. A 5 μm thick photoimageable BCB (Dow Product No. 4024-40) was used.

N-type silicon wafers, 100 mm in diameter with a 2400 Å thick silicon dioxide layer deposited on the surface, were used as substrates. The surface roughness was 1.5 nm as measured by the root-mean-square of bump height obtained with an atomic force microscope (AFM). The conductor metals used were evaporated 200 Å titanium and 3 μm copper.

The wafers were cleaned and the first layer of conductor was deposited and photo-patterned. This layer was followed by a 5 μ thick layer of liquid BCB, deposited by spin coating. Vias and streets in the BCB were then photo-patterned. After partially curing the BCB at 210°C, the second layer of conductor lines was photo-patterned. Finally, BCB was fully (hard) cured at 250°C. A detailed process for BCB may be found at the cyclotene Web site.

Because the BCB/Cu process was newly implemented at Sandia when the fabrication work for this study was performed, the metals were evaporated onto the wafer, rather than electroplated. As a result, the thickness of the metal layers was limited to 3 μm. The next generation of circuits using 15 μm thick copper deposited by electroplating is currently being investigated.

5 Results

The BCB/Cu HDI process was used to fabricate four stators simultaneously on four-inch wafers, as shown in Figures 4 and 5. To ensure high yield, only two layers of metal and one intervening layer of BCB were fabricated—enough to fabricate three-phase stators composed of split-level spiral coils. Dimensions of the individual conductors in the coils are shown in Figure 12. These dimensions are coincidentally almost identical to the conductor cross-section dimensions in [13]. As discussed in the previous section, the prototype stators were fabricated with evaporated metal, and therefore the thickness of the conductors was limited to 3 μm, which was verified by cross-section measurements. From the mask drawings, the phase resistance was calculated to be 88 Ω. The average phase resistance of the two motors (six measurements) used in the levitation tests described below was 88 Ω.

Tests were performed to determine the current-carrying capacity of the stators. The surface of a partially defective wafer was painted black and the wafer was mounted on a

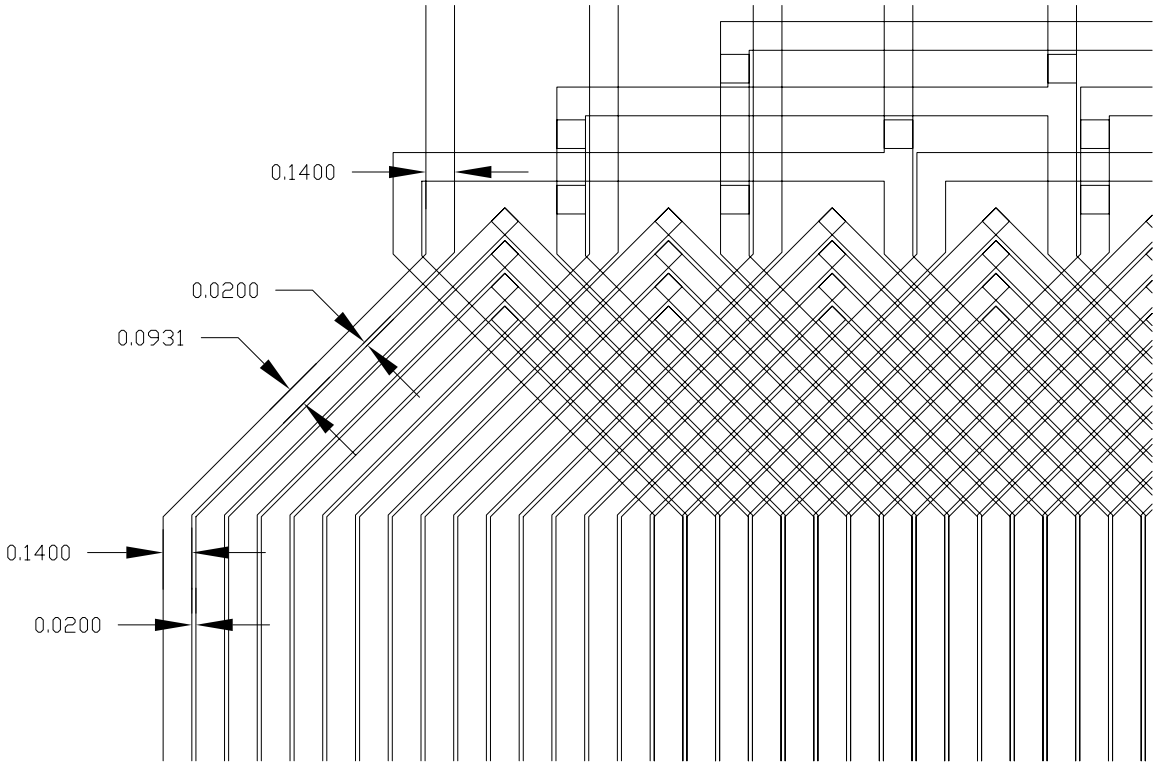

Figure 12: Conductor dimensions in the prototype actuator stator shown in millimeters. The gap between conductors is the minimum that can be achieved with the BCB/Cu HDI process at Sandia. Current density is maximum in the end turns where the conductors narrow (while maintaining the minimum gap).

block of aluminum on an infrared (IR) camera x-y stage using thermal grease. The IR camera was used to monitor the temperature of the stators while an increasing amount of power was applied to a phase of a stator. Power was applied until thermal steady-state was achieved. After each test, the wafer was allowed to cool and the phase resistances were verified to be unchanged from the beginning of the test.

Testing stopped when the limits of the power supply being used were reached. In the final test, 1.06 A flowed through one pole pitch of a phase and the peak steady-state temperature of the pole pitch was observed to be 107°C. The stator was undamaged by the test. At this peak current level, the current density in the end turns of the winding (the part of the winding with the smallest cross-section) was $4.2 \times 10^9 \mathrm{A/m^2}$. This current density is equivalent to flowing 213 A through a strand of 30 gauge wire. For reference, 30 gauge wire is rated at 0.8 A for a single wire in free air and 0.5 A for a bundle of wires. It may be that the intimate contact of the stator conductors with the silicon wafer (lower metal layer) and the BCB (upper metal layer) permits steady-state current densities

approximately two orders of magnitude greater than can be achieved with conventional wire. Similar results were obtained in [18].

Levitation tests were conducted to determine the current required to statically levitate the platen. A platen was levitated over the stators using two of the four stators (motors 2 and 4 in Figure 5). Motions in x and y were constrained. Servo loops were closed in the z direction using laser displacement sensors. The average direct current per motor required to levitate the platen 100 μm above the stator was measured to be $i_D = 138$ mA, which corresponds to three-phase currents of $i_A = -56.3$ mA, $i_B = -56.3$ mA, and $i_C = 112.5$ mA. (See Appendix H for details on computing three-phase currents from DQ currents.) The current required to statically levitate the platen is an order of magnitude below the maximum steady-state current the stator is capable of carrying.

The force model in [9] was used to calculate the current required to levitate the platen. When parameters for the actuator in the present study are used, the model predicts a direct current i_D of 96 mA. At first glance, the model (96 mA) and the experiment (138 mA) do not appear to be in good agreement. However, if the air gap is doubled to 200 μm, the model predicts a 114% increase in the direct current to $i_D = 109$ mA. The experimentally measured increase was 115%. This observation suggests that direct axes of platen magnet arrays were not properly aligned over the stator and that some of the measured direct current was, in fact, quadrature current. The normalized force production predicted by the model is 0.54 N/A, which is low because of the thinness of the stator windings. (Recall that only one metal layer pair was implemented in the prototype.) For thin stators, force production increases approximately linearly with the thickness of the windings. Therefore, a six-layer stator fabricated using electroplating with six 15 μm thick metal layers would produce approximately 8.8 N/A. Details of the model calculation may be found in Appendix D. Additional experimental results may be found in Appendix I.

6 Conclusions

The contribution of the this study is a planar multilayer polyphase coil architecture that provides for the lithographic implementation of efficient stator windings suitable for linear electric machines. A linear actuator was identified that can benefit from the precise lithographic fabrication of its stator windings in mesoscale implementations and possibly even in macroscale implementations. A mesoscale prototype was implemented using lithographically-fabricated stator windings.

The stator windings in the prototype actuator were implemented using a non-lapped BCB/Cu HDI process. Relative to lapped processes, this process is simple and inexpensive. The prototype stator was limited to thin copper layers (3 μm) due to the use of evaporated metal at the time of fabrication. More recently, investigations using electroplated metal have shown that BCB adequately replanarizes for metal traces up to 15 μm.

Tests showed that the stator windings are capable of handling very high current

densities (approximately $4 \times 10^9 \mathrm{A/m^2}$), providing sufficient current capacity for both levitation and translation. Levitation tests revealed force production that scales well to stators lithographically fabricated with thicker copper layers.

7 Future Work

Outstanding issues that need to be addressed include (a) the development of lithographic processes that yield substantially thicker metal layers and (b) a miniaturized feedback mechanism for commutating the motors and controlling the platen.

As discussed in previous sections, the BCB/Cu HDI process is a relatively simple process for fabricating traces of metal. It is currently being developed at Sandia for the interconnection of low-power, high-frequency circuitry. In addition to being self-replanarizing, BCB has excellent dielectric properties and low moisture uptake during and after processing. Development of the process has been focused on fabricating traces with well-defined impedances and on embedding passive components [20, 21]. More recently, customers funding development of the process have requested greater power-handling capability, and hence electroplating of the metal layers is currently being investigated [22]. This new process would greatly improve the performance of stators in magnetic actuators; force production would increase and power dissipation in the stator would decrease.

It is likely, however, that other processes will prove in the long run to be more suitable for the fabrication of magnetic actuator windings. Two processes stand out. First is a multi-layer LIGA process. For each layer the mold PMMA would need be removed and replaced with an electrical insulator with better thermal stability and higher thermal conductivity. After replanarization, a new layer of PMMA would be applied and the process repeated. Significant process development work would be necessary before a stator could be implemented in this way.

The second process that holds promise is based on SU-8. SU-8 is negative UV resist that allows the realization of high aspect ratio structures (though not has high as LIGA). With SU-8, conductors with a high aspect ratio cross-section could be fabricated using relatively standard lithography equipment (unlike LIGA). SU-8 was used to fabricate single-plane coils with conductors 12 μm wide and 64 μm thick in [15]. Consider that if the stators in the present study were implemented with conductors 64 μm thick (by 140 μm wide), a six metal layer stator would yield an astounding force production ratio of approximately 38 N/A and an excellent phase resistance of approximately 11 Ω. The problem with SU-8 is that it has a very poor thermal conductivity of 0.2 W/m-K (as does BCB and PMMA) and removing the irradiated SU-8 and replacing it with a high thermal conductivity electrical insulator is difficult because irradiated SU-8 is impervious to virtually all solvents [23]. As with the LIGA process above, significant process development work would be necessary before a stator could be fabricated using SU-8.

The other outstanding issue is development of a miniaturized feedback mechanism for commutating the motors and servoing the platen. Sensing the vertical displacement of the platen from the stator might be performed using capacitive sensors embedded in the

stator. The sensor interface circuitry could be embedded directly into the BCB layers. The work already performed on embedding passive components in the BCB layers points in this direction.

More challenging is sensing the lateral displacements of the platen. One idea is to mount Hall-effect sensors in the center space between the four motors (see Figure 5) that sense a small magnet array mounted at the center of the platen. Another idea is to implement miniature laser displacement sensors around the periphery of the actuator to measure the displacement away from each sensor, possibly using VCSELs. A third idea is mount optical structures on top surface of the platen through which lateral laser beams and detectors measure the displacement of the platen over the stator.

Finally, further development of MEMS magnetic actuators is contingent on finding a compelling application where a customer is willing to fund the additional development efforts described above. It is hoped that by pushing the size of the actuator into the mesoscale realm more application opportunities will arise.

A Actuator Parameters

Parameters for the actuator in this study are compiled here for reference.

- Nominal actuator throw = ± 3 mm in x and y.
- Nominal air gap $z_o = 100$ μm.
- Machine pole-pair pitch $l = 4.8$ mm.
- Machine fundamental wave number $\gamma_1 = 1309$ m^{-1}.

- Magnet array thickness $\Delta = 1.2$ mm.
- Magnet array width $w = 12$ mm.
- Number of magnet array pole-pair pitches $N_m = 2$.
- Magnet remanence (each magnet in the array) $B_r = 1.21$ T.

- Total mass of the platen (including 4 magnet arrays) = 10.59 g.
- Average mass of a glued magnet array = 1.225 g.
- Average mass of the magnets in an array = 1.213 g.
- Average mass of the glue in an array = 0.012 g.

- Number of stator phases = 3.
- Number of stator pole-pair pitches = 4.
- Stator winding thickness $\Gamma = 9.3$ μm.
- Stator winding pitch factor $k_p = 1$ (full pitch).
- Number of stator turns per pitch = 5.

- Stator conductor thickness (nominal) = 3 μm.
- Stator conductor pitch (coil center) = 160 μm.
- Stator conductor width (coil center) = 140 μm.
- Stator conductor-to-conductor gap (coil center) = 20 μm.

- Stator conductor pitch (end turns) = 113 μm.
- Stator conductor width (end turns) = 93 μm.
- Stator conductor-to-conductor gap (end turns) = 20 μm.
- Stator BCB thickness (nominal) = 3.8 μm.
- Stator turns density $\eta_o = 1.34 \times 10^9$ turns/m^2.

- Measured phase resistance (nominal) = 88 Ω.
- Peak current density (in the end turns) $J_p = 4.2 \times 10^9$ A/m^2.

- Motor geometric constant $G = 3.8 \times 10^{-10}$ m^3.

B Platen

The platen carries the actuator payload. Optimally, payloads would be passive and thus not require an umbilical cord, which might disturb the dynamics of the platen. In this study, the only payload carried by the platen was an aluminum cover plate.

A photograph of the surface of the platen that faces the wafer is shown in Figure 13. The four magnet arrays can be clearly seen that match the four stators on the wafer. A fabrication drawing for the magnet arrays is shown in Figure 14. The depth of the array is 12 mm. The cross-section dimensions of the inner magnets are 1.2 mm by 1.2 mm. The cross-section dimensions of the end magnets are 1.2 mm by 1.45 mm. The lengthening of the end magnets is to compensate for the truncation of the array and to improve the fundamental magnetization harmonic of the array. The separation features indicated on the drawing are a vestige of the manufacturing process and were used to keep track of the different types of magnets (A, B, and C) prior to magnetization.

The magnets in the array are made of sintered neodymium iron boron ($Nd_2Fe_{14}B$,

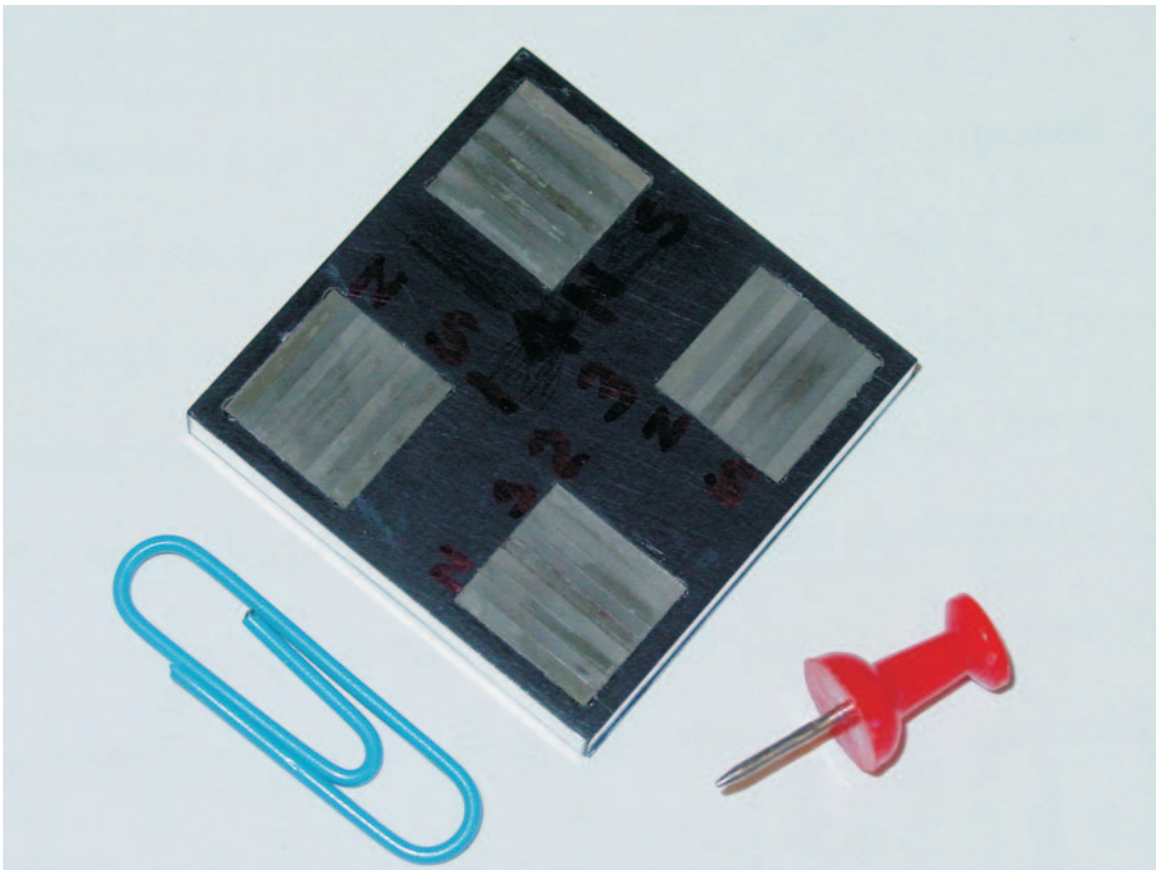

Figure 13: Four Halbach magnet arrays mounted in the platen.

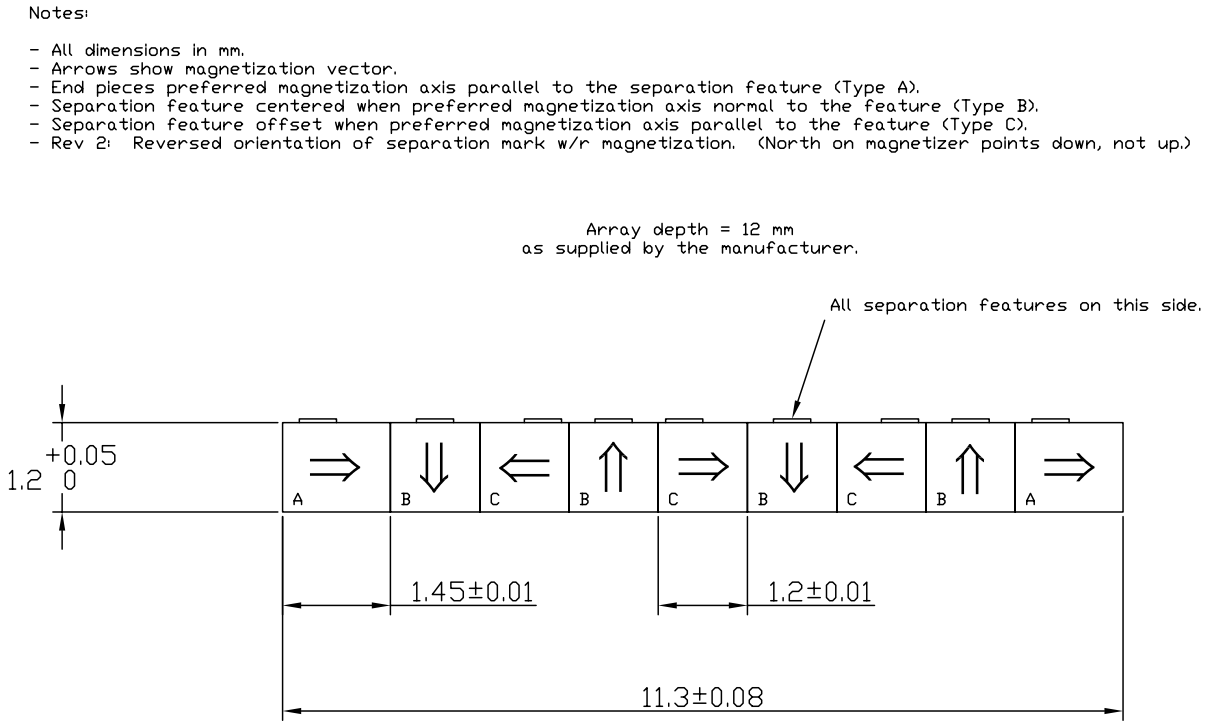

Figure 14: Halbach magnet array fabrication drawing.

or NdFeB for short). Bulk slabs of the material were purchased from the manufacturer[4] precision ground to 12 mm with the preferred direction of magnetization parallel to the grinding plane. The micro-EDM machine in division 14000 was used to cut 12 mm long magnets with multiple clockwise and counter-clockwise EDM passes until the desired tolerances were achieved, at which point a final cut was made to release the magnet from the slab. The imprecision of the final cut is evident in a visible separation mark that was used to identify the magnet type. Type A magnets were easy to identify by their non-square cross sections and they were cut from the bulk slab with the preferred direction of magnetization parallel to the surface with the separation mark. Type B magnets were cut from the bulk slab with the preferred direction of magnetization normal to the surface with the separation mark. Lastly, Type C magnets were cut from the bulk slab with the preferred direction of magnetization parallel to the surface with the separation mark, similar to the Type A magnets. Type B and Type C magnets were differentiated by the position of the separation mark, as shown in Figure 14. The separation mark on Type B magnets was centered on the magnet, while the separation mark on Type C magnets was offset.

[4]Magnetic Component Engineering, 2830 Lomita Blvd., Torrance CA 90505, http://www.mceproducts.com.

An LDJ 6607-1 magnetizer was used to magnetize the magnets.[5] The magnetizer was operated at its maximum pulse energy (7500 J) to ensure complete magnetization of the parts. A pole sensor was used to verify the correct magnetization of each part.

After magnetization, the individual magnets were assembled in-place in the windows of the platen shown in Figure 15. Assembly was facilitated by the use of a Teflon-coated steel backing plate on the stator side of the array. The backing plate served to hold the array in approximate position prior to gluing and clamping. Loctite 294 threadlocker was used to bond the array, since it is activated by iron, which is present in the NdFeB magnets. It was found that Loctite 294 adequately held the bonded arrays in the windows of the aluminum platen and thus a subsequent layer of epoxy to bond the arrays to platen was not applied.

Sintered neodymium iron boron is available in the highest energy products of all permanent magnet materials. Its chief competitor is samarium cobalt, which is available at slightly lower energy products, but with lower temperature coefficients and greater resistance to corrosion. Neither temperature nor corrosion were a concern for the actuator in the present study and so neodymium iron boron was the natural choice. It should also be noted that samarium cobalt is substantially more expensive than neodymium iron boron since cobalt is a strategic material, but due to the small volume of material required for the actuator in this study, cost was not a driver.

The specific magnet material used was N3578, which has a maximum energy product of 35 MG-Oe and a nominal remanence B_r at 20°C of 1.21 T. The nominal intrinsic coercivity H_{ci} of the material is 29 kOe. Choosing a material with a high intrinsic coercivity was important as the corners of the magnets in a Halbach array experience demagnetization (as will be discussed below). A material with a slightly higher energy product could have been chosen (around 40 MG-Oe), but as the energy product goes up, the intrinsic coercivity decreases, thereby increasing the risk of localized demagnetization in the magnet array.

The magnetization pattern shown in Figure 14 is known as a Halbach array. More precisely, it is a discrete Halbach array in that the magnetization vector of the array is rotated in 90° increments. In a continuous Halbach array, the magnetization vector is uniformly rotated in the array and the fundamental harmonic of the magnetic field on one side of the array is completely cancelled. The fundamental harmonic on the other side is enhanced by $\pi/2$ relative to a conventional array with the same pole pitch and where the magnetization vector is rotated in 180° increments [19]. The discrete Halbach array in Figure 14 is an approximation of a continuous Halbach array that is relatively easy to fabricate. In the discrete array the fundamental harmonic of the magnetic field on one side (the side away from the stator) is still completely eliminated and the fundamental on the other side (the side facing the stator) is enhanced to almost the same degree as a continuous Halbach array, namely $\sqrt{2}$. Halbach arrays were first reported in 1980 by Klaus Halbach [24] for beam shaping in particle accelerators. The usefulness of Halbach arrays in electric machines was not identified until more than a decade later by Trumper

[5]Walker LDJ Scientific, Rockdale Street, Worcester, MA 01606, http://www.walkerldj.com.

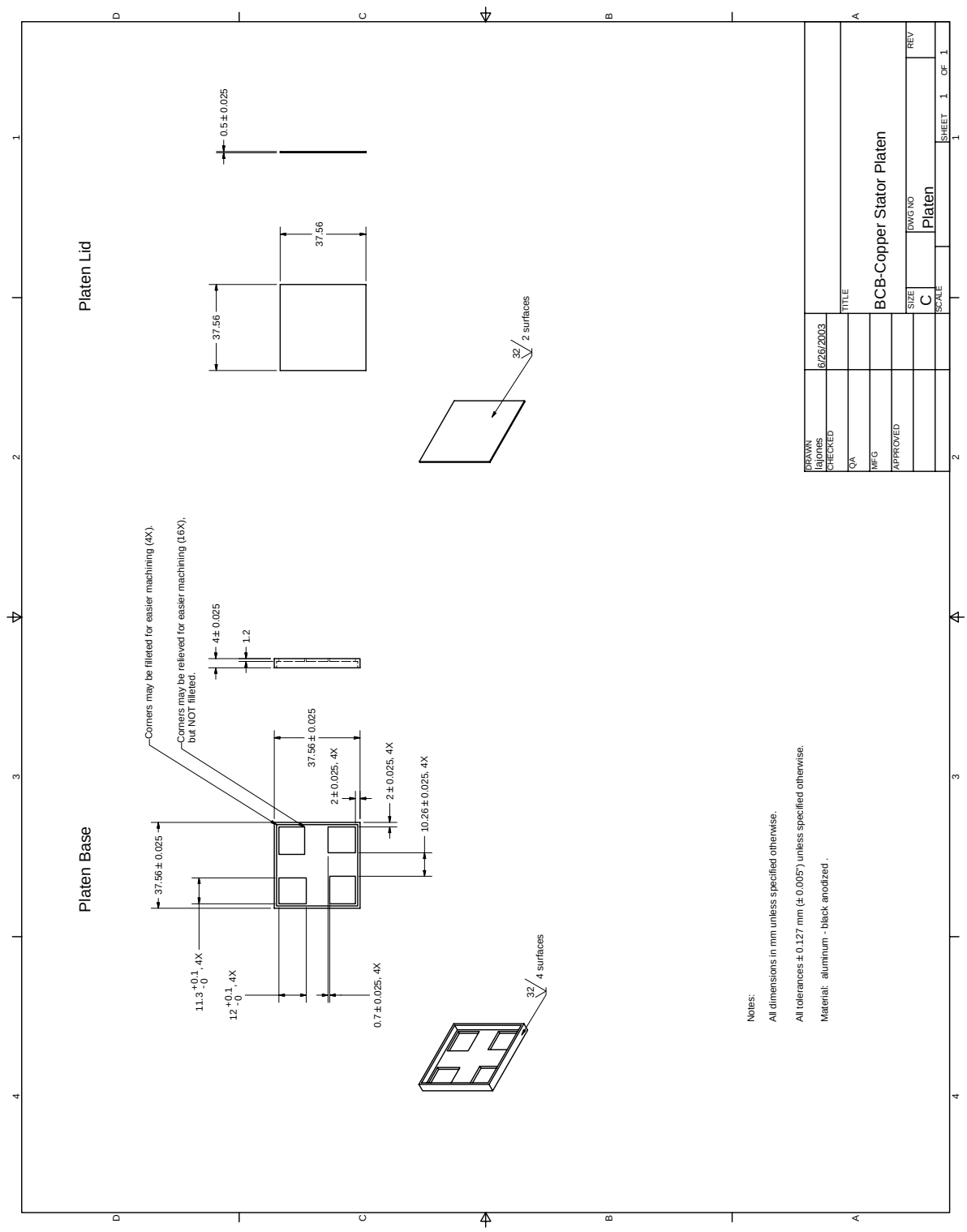

Figure 15: Fabrication drawing for the platen and the platen lid.

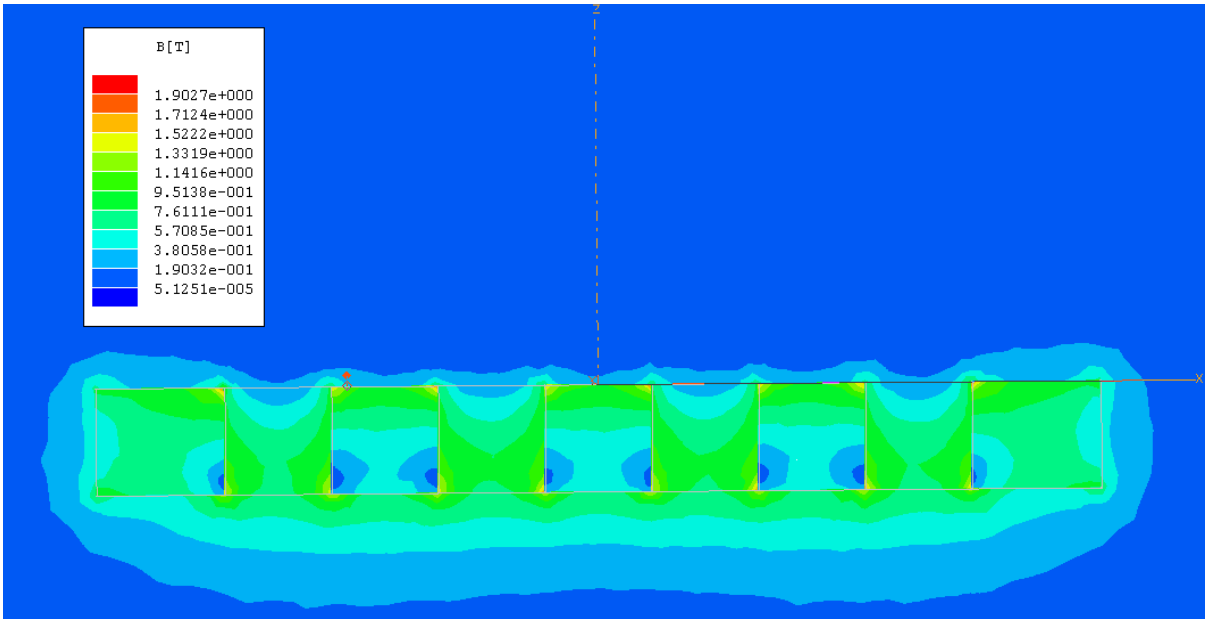

Figure 16: Finite element computation of the flux density of the Halbach magnet array in Figure 14.

in [19].[6]

The magnetic field produced by the array in Figure 14 was computed using Maxwell 3D by Ansoft.[7] A cross-section of the magnetic field down the middle of the array is shown in Figure 16 where it can be seen that the magnetic field is confined to one side of the array.

[6]It should be noted that Halbach arrays were applied to electric machines with no high-permeability materials in [19]. It has since been determined that conventional magnet arrays are superior when high-permeability materials are used to guide flux in the machine [25, 26]. The primary application of Halbach arrays in electric machines has been for linear machines that use integrated magnetic bearings, such as the actuator in the present study and, interestingly, magnetically-levitated trains [27].

[7]Ansoft Corporation, Four Station Square, Suite 200, Pittsburgh, PA 15219-1119, http://www.ansoft.com.

C Wafer Design

The planar windings were lithographically fabricated on four-inch silicon wafers in the CSRL. The complete design included six layers of metal and five intervening layers of BCB. Masks for the six metal layers are shown in Figures 17 through 22. The masks for the five intervening layers of BCB are not shown as they largely consist of vias between the metal layers.

Due to yield problems, only the first two layers of metal, with a single intervening layer of BCB were fabricated. Photographs of a wafer immediately after processing are shown in Figure 23. The active circuit area is approximately 6 cm^2 with 140 μm traces on a 160 μm pitch (20 μm line-to-line spacing) throughout.

Even after stopping at two metal layers, a wafer with four fully functional stators was not successfully fabricated. One wafer was completed with three fully functional stators and several wafers were completed with two fully functional stators. In the latter set, only two wafers had functional stators that were diagonal from each other (that is, either motors 1 and 3 or 2 and 4).

The failure modes observed in the stators were electrically open phases, abnormally high or low phase resistances, and phase-to-phase shorts. The source of these problems was often found to be contamination of the wafers by large dirt particles, rather than problems with the BCB process itself. Dirt particles ranging in size from tens of microns to hundreds of microns were found on the wafers. The dirt particles would either block the evaporated metal (open phases and high-resistance phases) or provide a bridge across traces during metal deposition (low-resistance phases and phase-to-phase shorts). As more experience was gained, cleanliness procedures were implemented that reduced the contamination problems. The situation will greatly improve when the new MESA facilities come on line. Examples of other wafer defects are shown in Figure 24.

Other fabrication lessons were learned with respect to the wafer designs. First, larger soldering pads should be used. Larger pads were included on metal layer six, but on the lower layers, 0402 surface-mount pads were used. While soldering 0402 surface-mount components is not difficult, soldering 30 gauge wires to 0402 pads proved to be much more difficult. Two wafers were lost to soldering problems caused by the pads on the lower layers being too small.

The second lesson is the importance of a final passivation layer. During normal operation of the actuator, a passivation layer was not necessary because of oxide layers that naturally form over both the stator conductors and the armature magnets. These oxide layers prevent the magnets from electrically shorting the windings. (Due to their iron content, NdFeB magnets have a moderate conductivity of approximately 144 $\mu\Omega$-cm—about the same as mercury.) During operation, however, control system upsets may cause the armature to impact the stator and break through these oxide layers. Such a failure was experienced and is described in Appendix I.

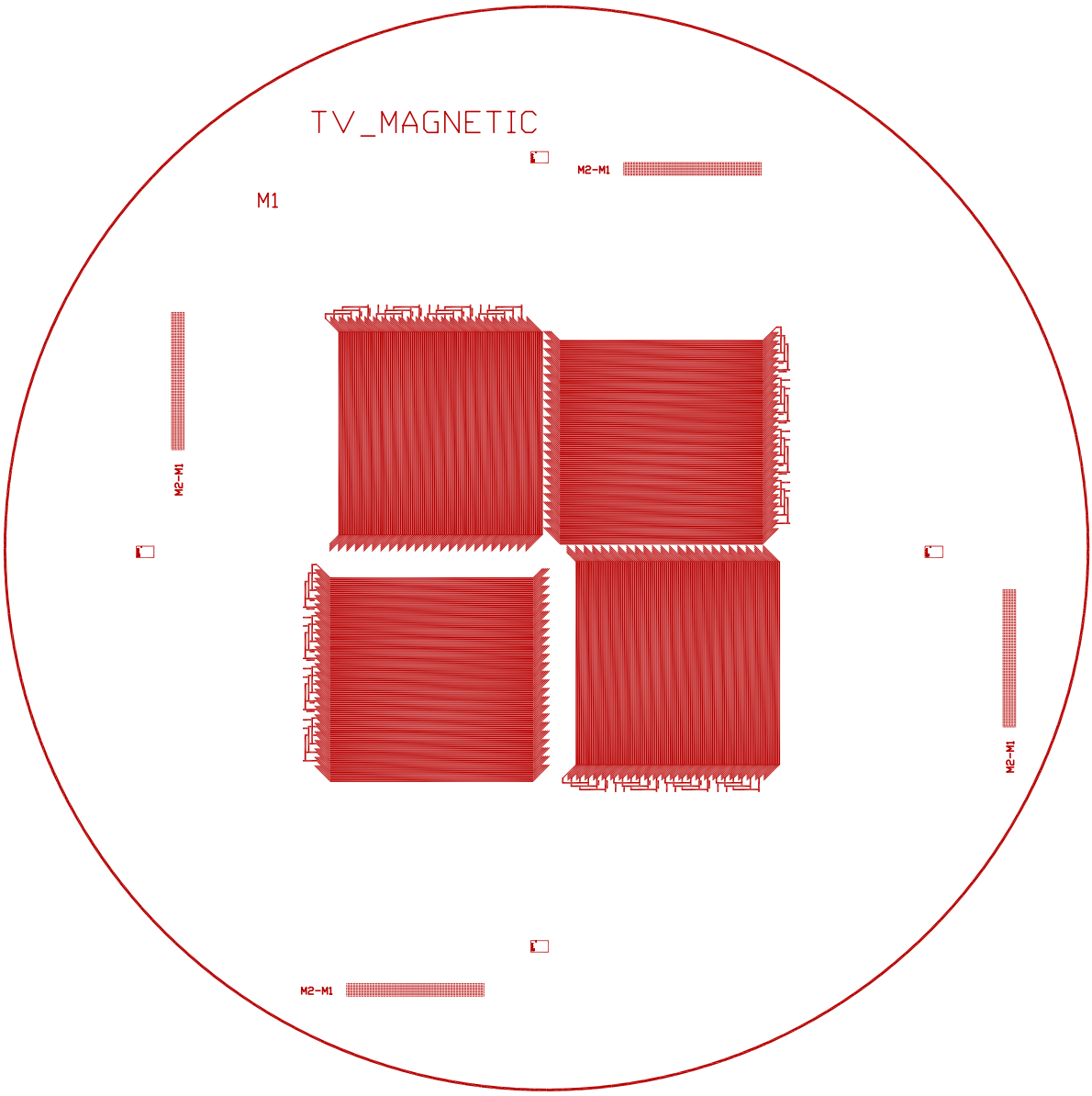

Figure 17: Mask for metal layer 1.

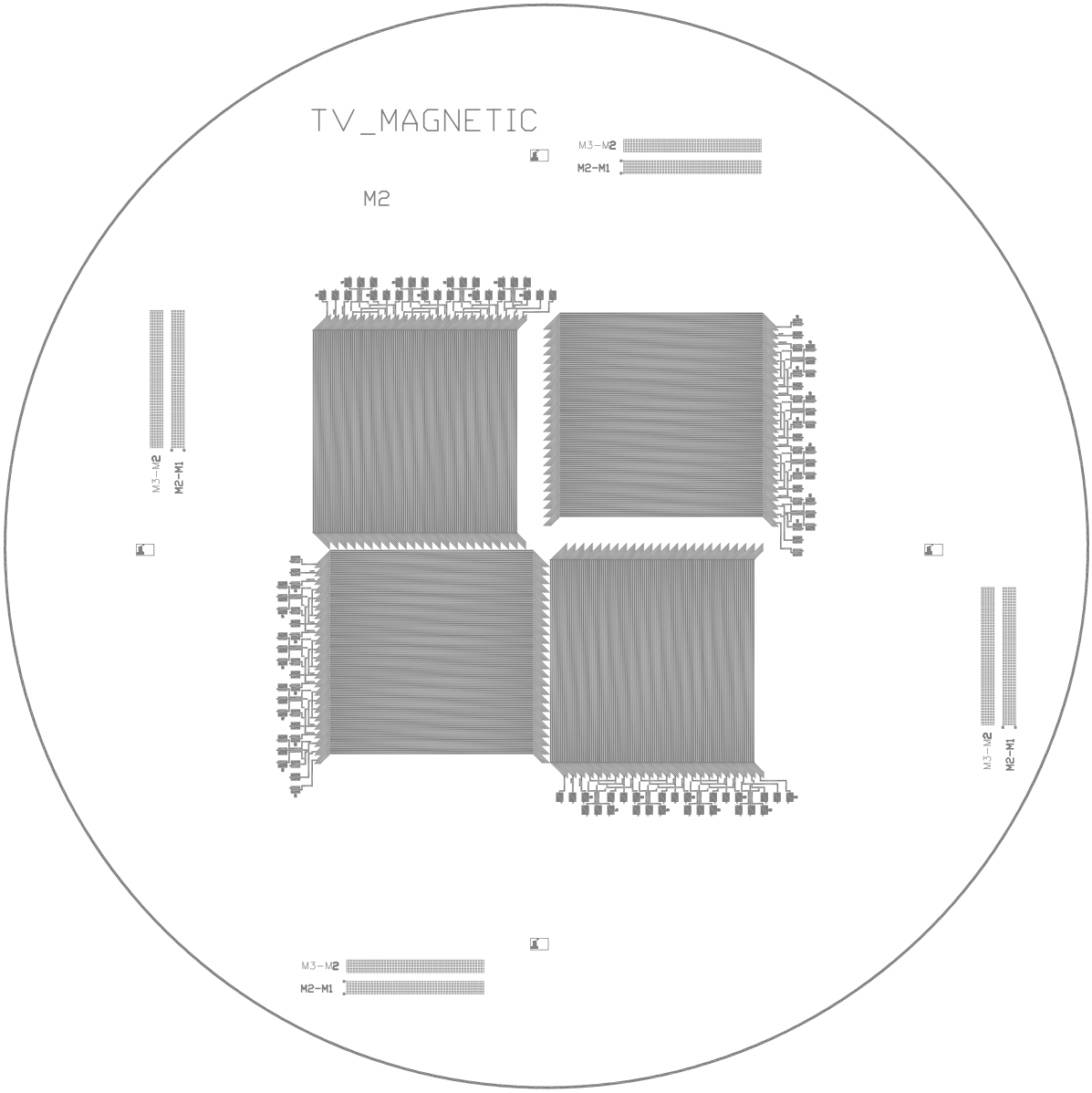

Figure 18: Mask for metal layer 2.

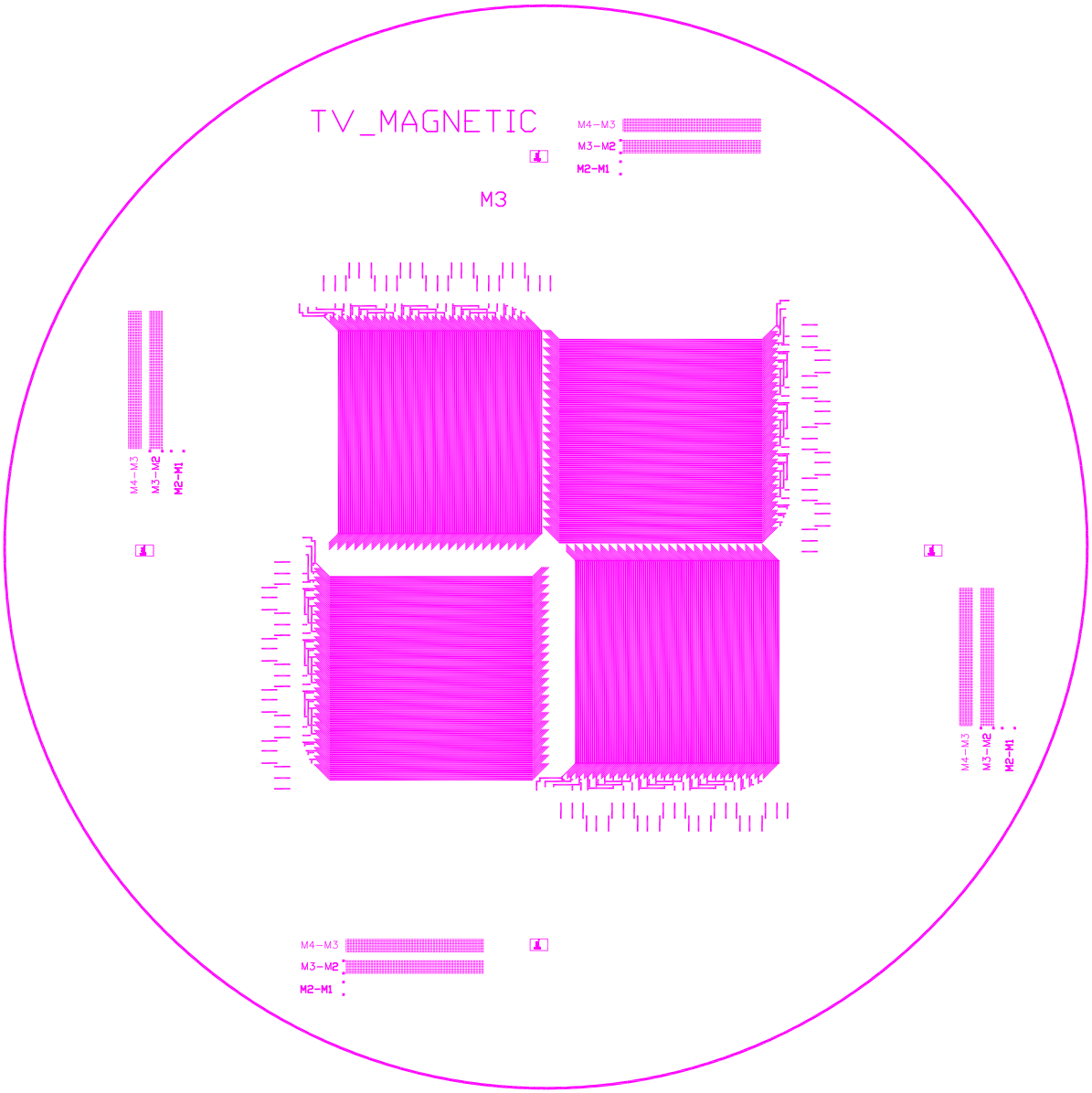

Figure 19: Mask for metal layer 3.

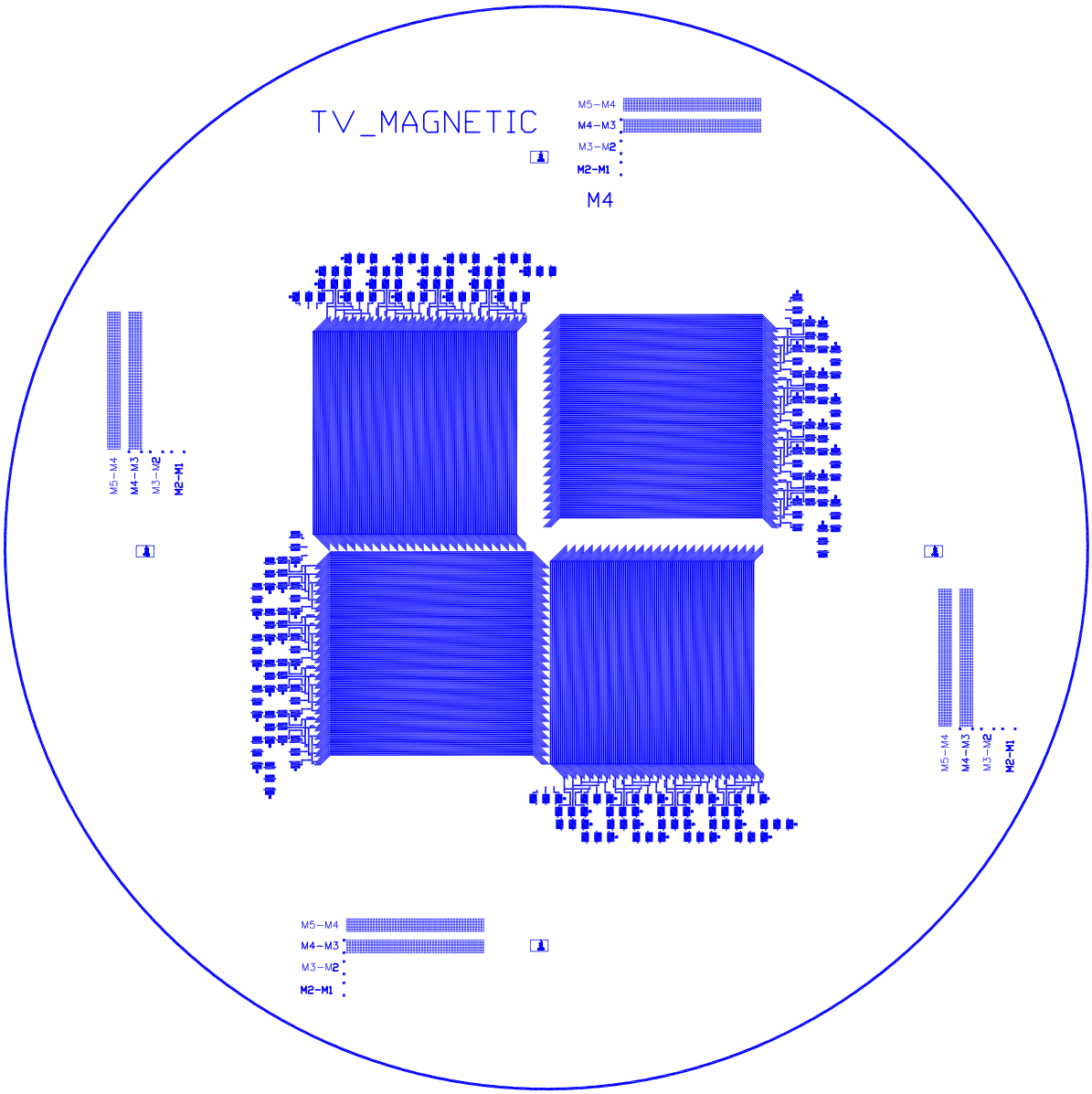

Figure 20: Mask for metal layer 4.

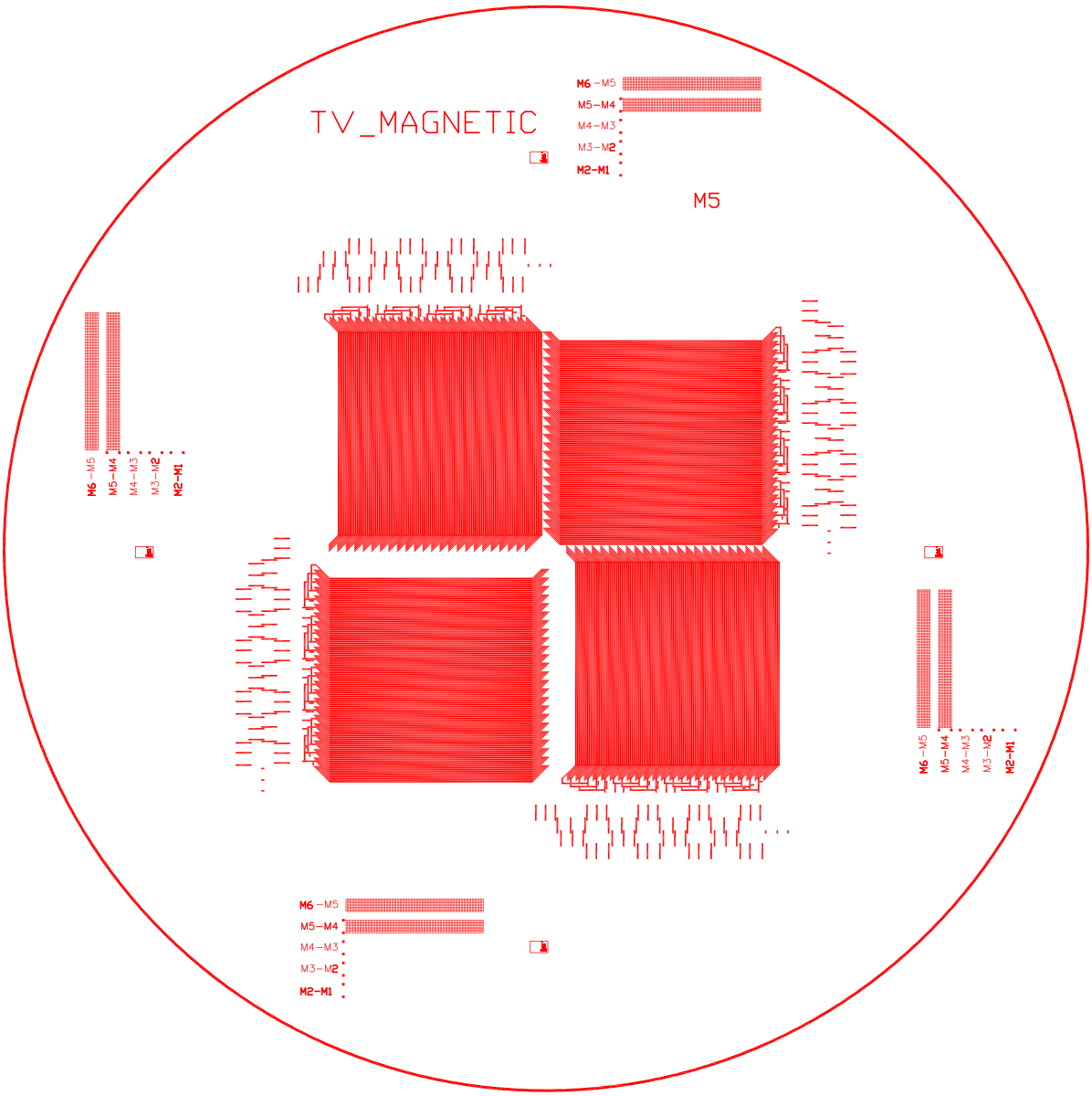

Figure 21: Mask for metal layer 5.

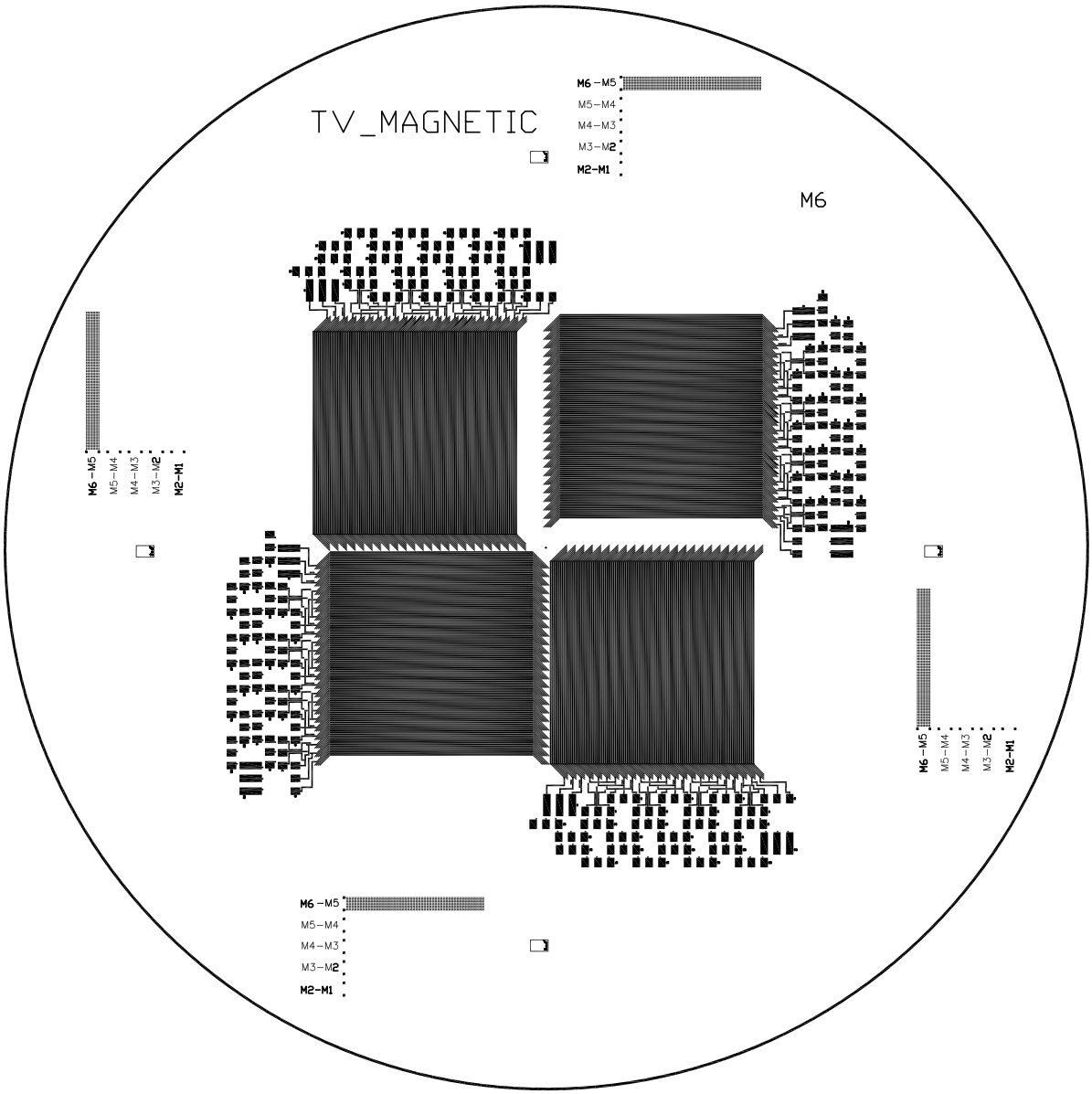

Figure 22: Mask for metal layer 6.

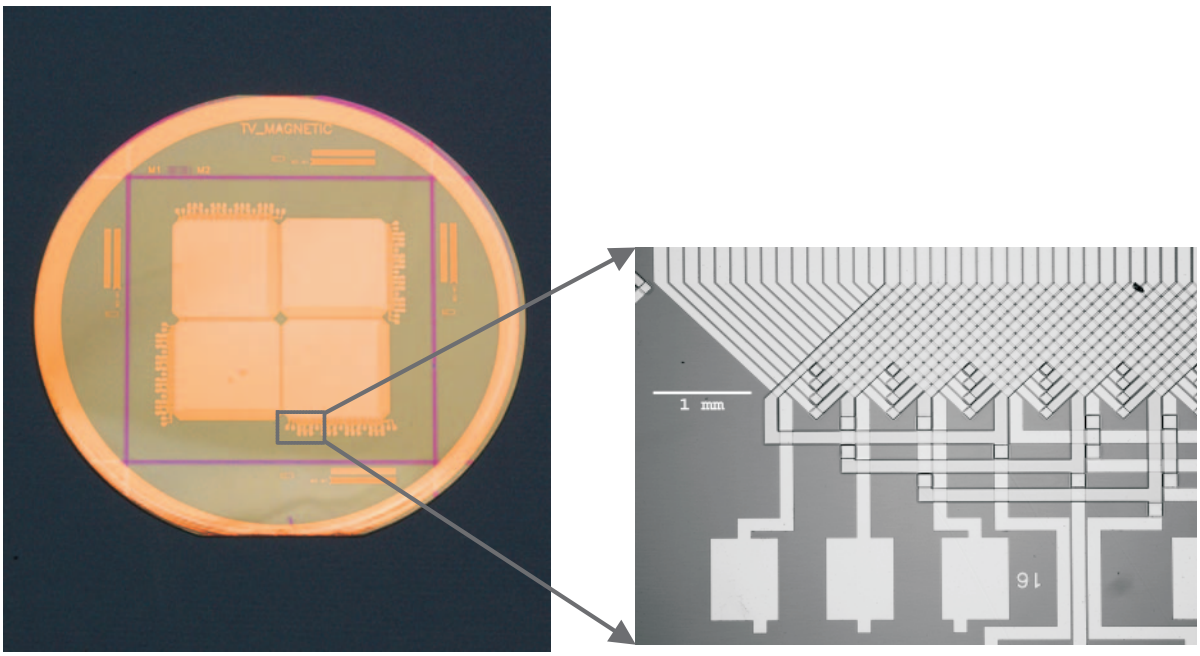

(a) (b)

Figure 23: (a) Wafer after processing the first two layers of metal with one intervening layer of BCB. (b) Magnified view showing the high density of the stator conductors.

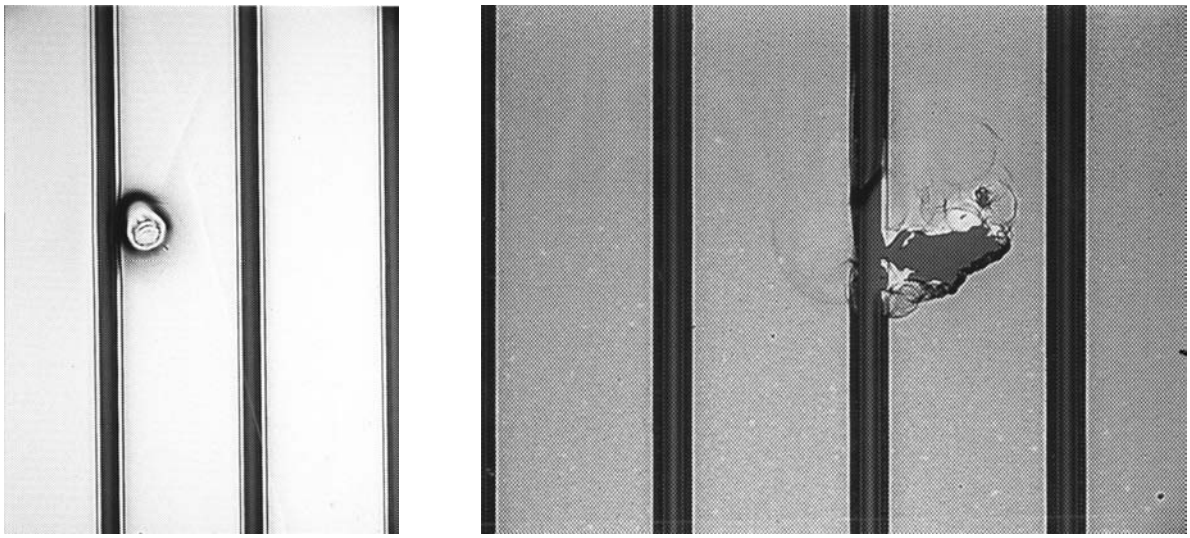

Figure 24: Examples of defects observed on the wafers.

D Force Modeling

The currents flowing through the stators in Figure 7, interact with the facing Halbach magnet arrays to generate Lorenz forces. In electric machine theory, the stator currents are typically decomposed into a current that generates force normal to the stator surface and a current that generates force tangent to the stator surface. These currents are known as the direct current and the quadrature current, respectively. In a rotary motor, direct currents act only to the compress the rotor about its axis and hence are undesirable.[8] High-performance rotary motor drives typically generate stator currents that have only a quadrature component.

In the levitated planar actuator of the present study, *direct* currents (i_D), which generate normal forces (f_n), are used to levitate the platen, and *quadrature* currents (i_Q), which generate tangential forces (f_t), are used to propel the platen laterally. Expressions relating these forces and currents are (adapted from [9])[9]

$$\begin{bmatrix} f_n \\ f_t \end{bmatrix} = \frac{1}{2} B_r \eta_o N_m G e^{-\gamma_1 z_o} \mathbf{K} \begin{bmatrix} i_D \\ i_Q \end{bmatrix}, \tag{5}$$

where B_r is the magnetic remanence of each magnet in the Halbach array (see Appendix B), η_o in the turns density of the stator, N_m is the number of pole pairs in the armature Halbach array, γ_1 is the absolute value of the wave number of the fundamental spatial harmonic in the machine ($k_1 = 2\pi/l$), z_o is the distance between the surface of the stator and the surface of the armature (the air gap), and

$$\mathbf{K} \equiv \begin{bmatrix} 1 & 0 \\ 0 & -1 \end{bmatrix} = \mathbf{K}^{-1}. \tag{6}$$

The constant G describes the geometry of the motor,

$$G = \frac{\sqrt{2}\omega l^2}{\pi^2} \left(1 - e^{-\gamma_1 \Gamma}\right) \left(1 - e^{-\gamma_1 \Delta}\right), \tag{7}$$

where ω is the length of the armature normal to the spatially varying magnetic field, Γ is the thickness of the stator windings, and Δ is the thickness of the armature Halbach array. These equations apply only to a machine with a Halbach array armature.

[8] Direct currents are sometimes used at high speeds to suppress the field of the armature magnets and hence reduce the back-emf induced in the stator.

[9] The expression relating force to current in [9] is

$$\begin{bmatrix} f_n \\ f_t \end{bmatrix} = \frac{1}{2} B_r \eta_o N_m G e^{-\gamma_1 z_o} \begin{bmatrix} -\sin(\gamma_1 x_o) & \cos(\gamma_1 x_o) \\ \cos(\gamma_1 x_o) & \sin(\gamma_1 x_o) \end{bmatrix} \begin{bmatrix} i_a \\ i_b \end{bmatrix},$$

where the a axis at $x_o = 0$ is aligned with the peak current density in the stator. Axis b leads a spatially in x_o. In conventional electric machine theory, the $\alpha\beta$ axes are used. These axes are aligned with the peak magnetic field in the stator. Hence, the $\alpha\beta$ axes lead the ab axes by $\pi/2$. Therefore, $i_a = -i_\beta$ and $i_b = i_\alpha$. Making these substitutions in the equation above and then using (40) yields equation (5).

Numerous design insights may be gleaned from the above equations and therefore it is worth discussing them in more detail. First, the expressions relating direct current to normal force and quadrature current to tangential force are identical in magnitude *and* independent. This is because, by design, current at any point in the stator is normal to the magnetic field. The direction of the force vector at any point is thus determined by the direction of the armature magnetic field. The armature magnetic field can be resolved into two orthogonal components, both normal to the current: armature magnetic field tangential to the plane of the stator and armature magnetic normal to the plane of the stator. Where the armature magnetic field is tangential to the plane of the stator, the force is normal and the current is direct current. Where the armature magnetic field is normal to the plane of the stator, the force is tangential and the current is quadrature current. Throughout most of the stator, the armature magnetic field has both tangential and normal components, and hence the stator current has non-zero direct and quadrature components.

Equations (5) and (7) reveal ways in which the force produced by the actuator can be increased. In (5), increasing the remanence B_r of the magnets in the Halbach array, increasing the stator turns density η_o (which for a given terminal in current, is equivalent to increasing the stator current density), and increasing the number of pole-pair pitches N_m in the armature will increase both the normal and tangential force production of the actuator.

In (7), increasing the depth w of the Halbach arrays will increase the force produced by the actuator, and force production increases with the *square* of the fundamental spatial harmonic length l.[10] Increasing the thickness Γ of the stator windings and the thickness Δ of the armature also increases force production, but with exponentially diminishing returns. For thin stators and armatures, the exponentials in (7) can be replaced with their first order expansions ($e^x \approx 1+x$, for small x), and hence force production increases approximately linearly with stator and armature thickness, as was claimed in Section 5. Equation (5) was used in [19] to deduce that the power optimal thickness of the stator windings in a synchronous machine with Halbach arrays is one-fifth the fundamental spatial period of the magnetic field in the machine. The optimal thickness of the armature Halbach array is discussed in Appendix B.

Substituting parameters from Appendix A yields $G = 3.8 \times 10^{-10}$ m^3. When the air gap z_o between the stator and platen is 100 μm,

$$\begin{bmatrix} f_n \\ f_t \end{bmatrix} = \quad 0.54\,\mathbf{K} \begin{bmatrix} i_D \\ i_Q \end{bmatrix}. \tag{8}$$

For two motors to statically levitate the platen, each motor must generate 52 mN, and (8) predicts that 96 mA of direct current will be required.

[10] As the pole-pair pitch l is increased in this type of machine, force production increases because more of the armature magnetic field couples with the stator instead of fringing in the air gap. In machines that use high-permeability materials to steer the flux, force production typically *decreases* as the pole-pair pitch is increased.

E Dynamics

Linearized dynamics of the actuator are derived in this appendix. A derivation is performed here for completeness and because there is a small error in the tangential dynamics reported in [9].

The nonlinear forces in (5) may be linearized by retaining zeroth and first-order terms of Taylor expansions about a static operating point. Assume the following perturbations about a static operating point

$$z_o = \bar{z}_o + \tilde{z}_o \,, \tag{9}$$

$$i_D = \bar{\imath}_D + \tilde{\imath}_D \,, \tag{10}$$

$$i_Q = \bar{\imath}_Q + \tilde{\imath}_Q \,. \tag{11}$$

When the z axis of the actuator is aligned with the gravity vector, then in the static condition $\bar{\imath}_D \neq 0$ and $\bar{\imath}_Q = 0$. Alternatively, when the actuator is oriented such that the x or the y axis is aligned with the gravity vector, then $\bar{\imath}_D = 0$ and $\bar{\imath}_Q \neq 0$.

Consider the linearization of the normal force f_n in (5). To first order

$$\begin{aligned} f_n(z_o, i_D) &\approx f(\bar{z}_o, \bar{\imath}_D) + \tilde{z}_o \left.\frac{\partial f}{\partial z_o}\right|_{i_D} (\bar{z}_o, \bar{\imath}_D) + \tilde{\imath}_D \left.\frac{\partial f}{\partial i_D}\right|_{z_o} (\bar{z}_o, \bar{\imath}_D) \\ &= \frac{1}{2} B_r \eta_o N_m G \left[e^{-\gamma_1 \bar{z}_o} \bar{\imath}_D - \gamma_1 e^{-\gamma_1 \bar{z}_o} \bar{\imath}_D \tilde{z}_o + e^{-\gamma_1 \bar{z}_o} \tilde{\imath}_D \right] . \end{aligned} \tag{12}$$

Assuming the actuator is oriented with the plane of the stator normal to the gravity vector, Newton's second law applied to the system with all four motors providing normal forces yields

$$M \frac{d^2 \tilde{z}_o}{dt^2} = 2 B_r \eta_o N_m G \left[e^{-\gamma_1 \bar{z}_o} \bar{\imath}_D - \gamma_1 e^{-\gamma_1 \bar{z}_o} \bar{\imath}_D \tilde{z}_o + e^{-\gamma_1 \bar{z}_o} \tilde{\imath}_D \right] - Mg \,, \tag{13}$$

where M is the mass of the platen and g is the earth's gravitational acceleration. In the static condition, the force generated by the nominal current $\bar{\imath}_D$ offsets the force of gravity, and hence a linear, second-order, differential equation describing the small-signal normal dynamics results,

$$M \frac{d^2 \tilde{z}_o}{dt^2} + 2 B_r \eta_o N_m G \gamma_1 e^{-\gamma_1 \bar{z}_o} \bar{\imath}_D \tilde{z}_o = 2 B_r \eta_o N_m G e^{-\gamma_1 \bar{z}_o} \tilde{\imath}_D \,. \tag{14}$$

A spring-mass system with zero damping may be recognized, driven by the sum of the small-signal normal motor forces, that is,

$$M \frac{d^2 \tilde{z}_o}{dt^2} + M \omega_o^2 \tilde{z}_o = \sum_{k=1}^{4} \tilde{f}_{nk} \,. \tag{15}$$

By equating terms in (14) and (15), and using the parameters in Appendix A, the open-loop natural frequency $f_o = \omega_o / 2\pi$ of the gap dynamics is calculated to be 25.5 Hz. The

dynamics are stable, albeit with no damping, only marginally so. These dynamics were used to design the vertical servo controllers described in Appendix F.

Linearization of the lateral dynamics is more subtle because lateral motion is implicit in the expression for tangential force f_t in (5). Lateral motion reappears in (5) when the quadrature current i_Q is referred to the stator frame using (40) or (41). Using (40), the tangential force in terms of stator currents is

$$f_x(x_o, i_\alpha, i_\beta) = -\frac{1}{2} B_r \eta_o N_m G e^{-\gamma_1 z_o} \left[-\sin(\gamma_1 x_o) i_\alpha + \cos(\gamma_1 x_o) i_\beta \right] . \tag{16}$$

Assuming perturbations of the form

$$x_o = \bar{x}_o + \tilde{x}_o \,, \tag{17}$$
$$i_\alpha = \bar{\imath}_\alpha + \tilde{\imath}_\alpha \,, \tag{18}$$
$$i_\beta = \bar{\imath}_\beta + \tilde{\imath}_\beta \,, \tag{19}$$

the first-order linearization of f_x is

$$f_x(x_o, i_\alpha, i_\beta) \approx \tag{20}$$
$$-\frac{1}{2} B_r \eta_o N_m G e^{-\gamma_1 \bar{z}_o} \Big(\left[-\sin(\gamma_1 \bar{x}_o) \bar{\imath}_\alpha + \cos(\gamma_1 \bar{x}_o) \bar{\imath}_\beta \right] + \tag{21}$$
$$\gamma_1 \tilde{x}_o \left[-\cos(\gamma_1 \bar{x}_o) \bar{\imath}_\alpha - \sin(\gamma_1 \bar{x}_o) \bar{\imath}_\beta \right] + \left[-\sin(\gamma_1 \bar{x}_o) \tilde{\imath}_\alpha + \cos(\gamma_1 \bar{x}_o) \tilde{\imath}_\beta \right] \Big) . \tag{22}$$

The grouped trigonometric terms may be recognized as direct and quadrature currents, and hence,

$$f_x(x_o, i_\alpha, i_\beta) \approx -\frac{1}{2} B_r \eta_o N_m G e^{-\gamma_1 \bar{z}_o} \left(\bar{\imath}_Q - \gamma_1 \tilde{x}_o \bar{\imath}_D + \tilde{\imath}_Q \right) . \tag{23}$$

Assuming the actuator is oriented with the plane of the stator normal to the gravity vector, then $\bar{\imath}_Q = 0$ at the static operating point. Newton's second law applied to the system with two motors providing tangential forces in the x direction yields

$$M \frac{d^2 \tilde{x}_o}{dt^2} - B_r \eta_o N_m G \gamma_1 e^{-\gamma_1 \bar{z}_o} \bar{\imath}_D \tilde{x}_o = -B_r \eta_o N_m G e^{-\gamma_1 \bar{z}_o} \tilde{\imath}_Q \,. \tag{24}$$

This result is the same as the tangential dynamics derived in [9, eq. 16] except for the γ_1 parameter multiplying the spring term and the minus sign on the right side of the equation above. A spring-mass system with zero damping may be recognized, driven by the sum of the small-signal normal motor forces, that is,

$$M \frac{d^2 \tilde{z}_o}{dt^2} - M \omega_o^2 \tilde{z}_o = \sum_{k \in \{1,3\}} \tilde{f}_{tk} \,. \tag{25}$$

Unlike the normal dynamics, the undriven tangential dynamics are unstable.

It is interesting to note the similarity of the normal and tangential dynamics in (14) and (24), respectively. This similarity is a result of the expressions relating direct current

to normal force and quadrature current to tangential force in (5) being identical in magnitude and independent, as was noted in Appendix D. It is also interesting to observe the effect of rotating the actuator so that either its x or y axis is aligned with the gravity vector. In this case, $\bar{\imath}_Q$ is not zero as the tangential forces must balance the mass of the platen. However, $\bar{\imath}_D$ is zero and hence the spring forces in both (14) and (24) are zero. The dynamics are now stable with simple double poles at the origin.

F Control

The platen may be controlled as a rigid body with six degrees of freedom. Six servo loops are needed for the three translation dynamic states and the three rotation dynamic states of the platen. Accordingly, six measurements of the platen are required to establish its position and attitude in space. Three laser displacement sensors were positioned over motors 1, 3, and 4 to measure the vertical displacement of the platen and its rotations about the x and y axes. One laser displacement sensor was used to measure the lateral displacement of the platen in x and two sensors were used to measure the lateral displacement of the platen in y and its rotation about the z axis.

Typically, the position of the platen center of mass is controlled along with rotations about the center of mass. In this study, the vertical lasers were instead used to close three servo loops around the platen height measured over motors 1, 3, and 4, using each respective motor. As a result, the plane of the platen (the z plane) was directly servoed. Commanding rotations about the x and y axes required a software mapping of the motion onto the z plane, thereby generating vertical position commands for motors 1, 3, and 4. The other three servo loops controlled translation in x, translation in y, and rotation about z.

Lead-lag compensators were used to target a closed-loop bandwidth of 100 Hz while sampling at 10 kHz. The lead zero was set at 60 Hz, the lead pole at 600 Hz, the lag zero at 6 Hz and the lag pole at 0.6 Hz. Using (14) for the normal dynamics and the parameters in Appendix A, the compensator which yields a damping ratio of 0.5 is

$$G_{zn}(s) = 2 \times 10^4 \left(\frac{s + 377}{s + 3770} \right) \left(\frac{s + 37}{s + 3.7} \right) . \tag{26}$$

The dominant poles are at $-234 \pm j406$ rad/s. The loop transmission is shown in Figure 25, and good stability is indicated. The closed-loop response is shown in Figure 26 and the step response in Figure 27. A similar analysis was carried out for the tangential and torsional dynamics.

The six compensators generate six force and torque commands,

$$\begin{bmatrix} f_{zp1} \\ f_{zp3} \\ f_{zp4} \\ f_{xp} \\ f_{yp} \\ \tau_{zp} \end{bmatrix} . \tag{27}$$

The last three commands (f_{xp}, f_{yp}, τ_{zp}) must be allocated amongst the four motors.

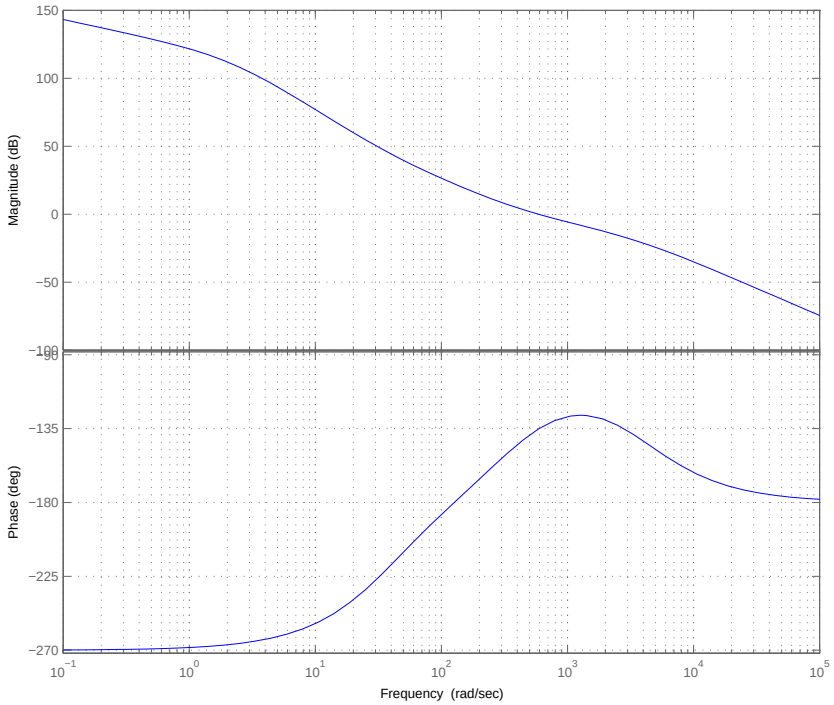

Figure 25: Vertical servo model loop transmission.

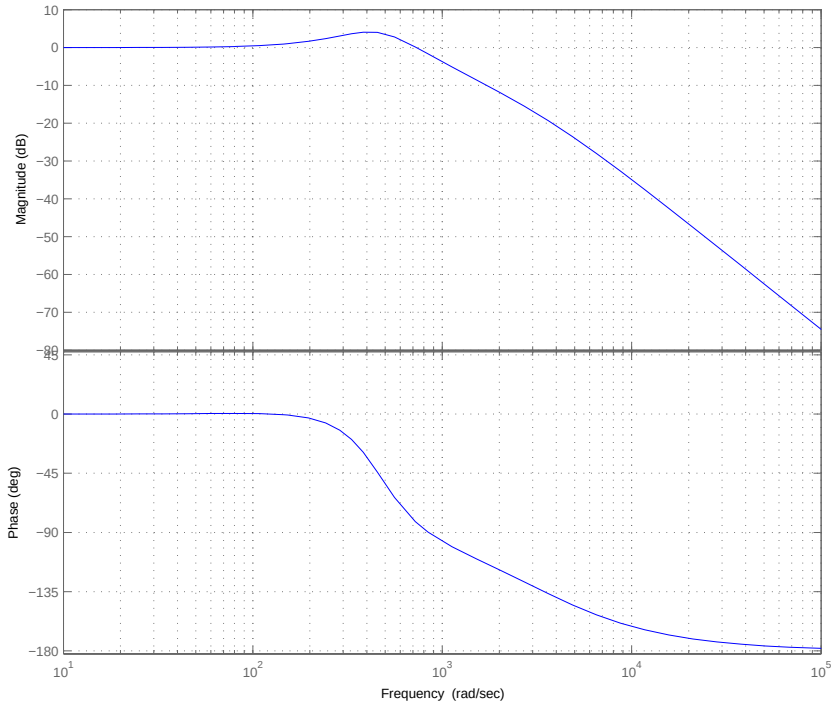

Figure 26: Vertical servo model closed-loop response.

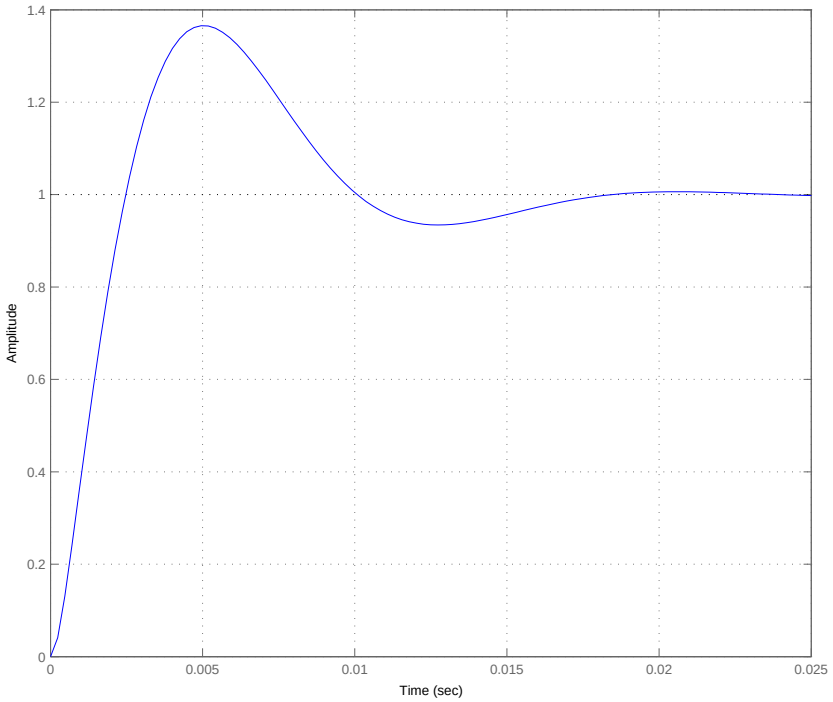

Figure 27: Vertical servo model step response.

G Force Allocation

The force and torque outputs from the compensators in Appendix F must be allocated between the four motors. Because the platen is symmetric in x and y, the normal forces required to support the weight of the platen are allocated equally amongst the four motors,

$$f_{zn} = \frac{Mg}{4} + f_{zpn}, \quad n \in \{1, 2, 3, 4\}\,. \tag{28}$$

Tangential forces in x and y are allocated to the motors capable of producing these forces,

$$f_{xn} = \frac{1}{2} f_{xpn}, \quad n \in \{1, 3\}\,, \tag{29}$$

$$f_{yn} = \frac{1}{2} f_{ypn}, \quad n \in \{2, 4\}\,. \tag{30}$$

Torque about the z axis requires the allocation of tangential forces and motors 2 and 4 are (arbitrarily) used to generate this torque. Referring to Figure 28,

$$\begin{bmatrix} f_{x1} \\ f_{x3} \\ f_{y2} \\ f_{y4} \end{bmatrix} = \frac{1}{2} \begin{bmatrix} 0 \\ 0 \\ \tau_{zp}/l_s \\ -\tau_{zp}/l_s \end{bmatrix}, \tag{31}$$

where $l_s = 10.78$ mm. Although tilt torques about the horizontal axes x and y are not used (since the z plane is commanded directly), for completeness expressions are included here for allocating tilt torque commands to the normal forces of the four motors. Referring again to Figure 28,

$$\begin{bmatrix} f_{z1} \\ f_{z2} \\ f_{z3} \\ f_{z4} \end{bmatrix} = \frac{1}{2\left(l_l^2 + l_s^2\right)} \begin{bmatrix} l_l\tau_{yp} + l_s\tau_{xp} \\ l_l\tau_{xp} - l_s\tau_{yp} \\ -l_l\tau_{yp} - l_s\tau_{xp} \\ l_s\tau_{yp} - l_l\tau_{xp} \end{bmatrix} \tag{32}$$

where $l_s = 10.78$ mm and $l_l = 11.13$ mm.

Summarizing, the force commands to the motors are

$$\begin{bmatrix} f_{z1} \\ f_{z2} \\ f_{z3} \\ f_{z4} \end{bmatrix} = \frac{Mg}{4} + \begin{bmatrix} f_{zp1} \\ f_{zp2} \\ f_{zp3} \\ f_{zp4} \end{bmatrix} \tag{33}$$

$$\begin{bmatrix} f_{x1} \\ f_{x3} \\ f_{y2} \\ f_{y4} \end{bmatrix} = \frac{1}{2} \begin{bmatrix} f_{xp} \\ f_{xp} \\ f_{yp} + \tau_{zp}/l_s \\ f_{yp} - \tau_{zp}/l_s \end{bmatrix}. \tag{34}$$

The phase currents required in each motor to generate these forces are then computed, as described in Appendix H.

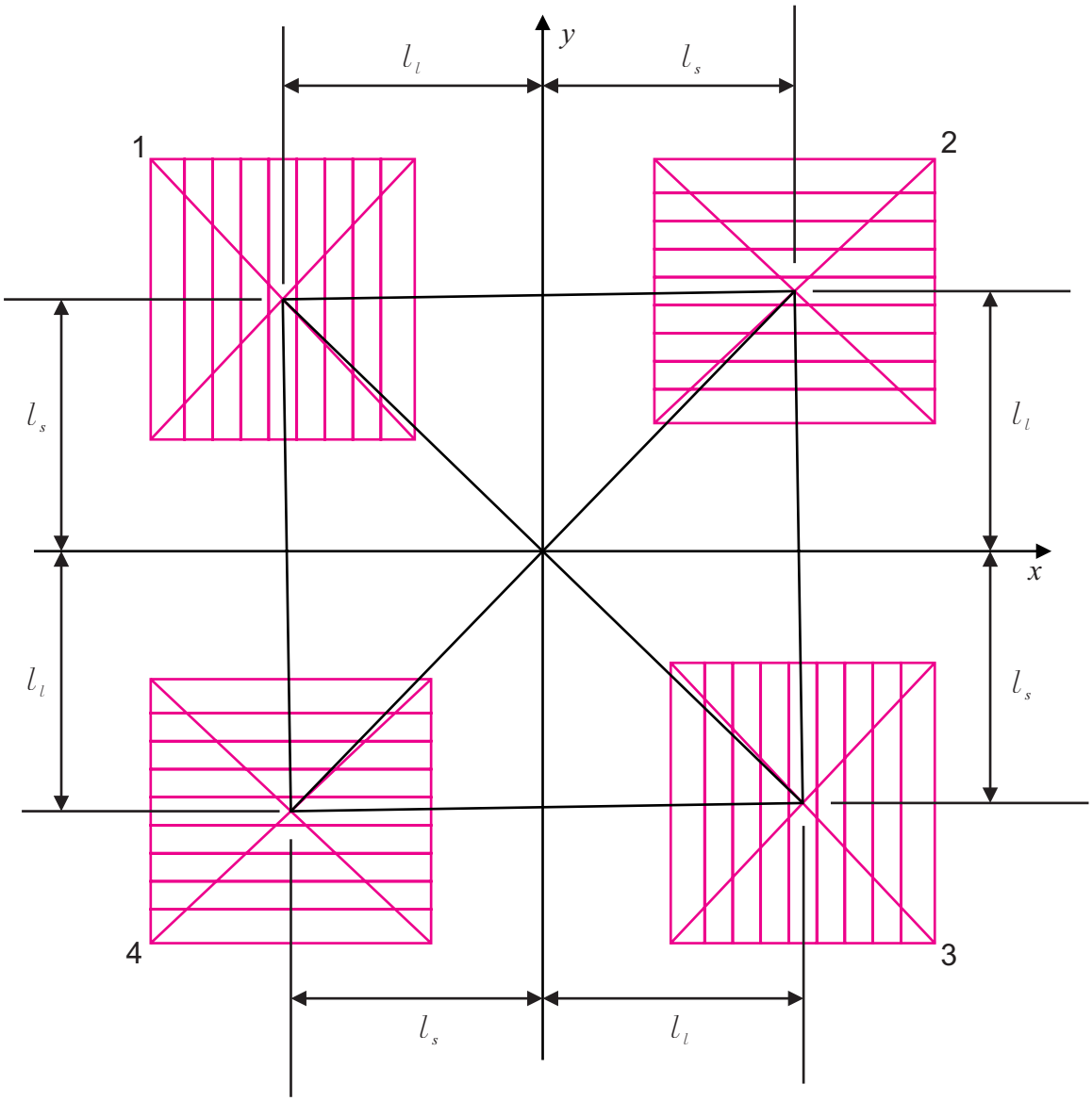

Figure 28: Overhead view of the magnet arrays in the platen. The origin is at the center of mass of the platen. The centers of mass of the arrays are offset by l_s and l_l where $l_s \neq l_l$.

H Commutation

After forces from the controllers have been allocated to the individual motors, current commands must be generated for the current amplifiers. Direct and quadrature currents may be calculated by inverting (5),

$$\left[\begin{array}{c} i_{Dn} \\ i_{Qn} \end{array} \right] = \frac{2e^{\gamma_1 z_o}}{B_r \eta_o N_m G} \mathbf{K} \left[\begin{array}{c} f_{zn} \\ f_{(x\|y)n} \end{array} \right], \tag{35}$$

where n specifies a particular motor. Recall that motors 1 and 3 generate tangential forces in the x direction and motors 2 and 4 generate tangential forces in the y direction, hence the boolean OR notation in $f_{(x\|y)n}$.

Direct and quadrature currents are in the rotor frame and hence must be referred to the orthogonal currents i_α and i_β in the stator frame. For motors 1 and 3 ($n \in \{1, 3\}$),

$$\left[\begin{array}{c} i_\alpha \\ i_\beta \end{array} \right] = e^{\gamma_1 x_o \mathbf{J}} \left[\begin{array}{c} i_D \\ i_Q \end{array} \right], \tag{36}$$

and for motors 2 and 4 ($n \in \{2, 4\}$)

$$\left[\begin{array}{c} i_\alpha \\ i_\beta \end{array} \right] = e^{\gamma_1 y_o \mathbf{J}} \left[\begin{array}{c} i_D \\ i_Q \end{array} \right]. \tag{37}$$

The matrix $\mathbf{J}$ is defined as[11]

$$\mathbf{J} \equiv \left[\begin{array}{cc} 0 & -1 \\ 1 & 0 \end{array} \right] \tag{38}$$

and the rotation resolves to

$$e^{\gamma_1 x_o \mathbf{J}} = \left[\begin{array}{cc} \cos(\gamma_1 x_o) & -\sin(\gamma_1 x_o) \\ \sin(\gamma_1 x_o) & \cos(\gamma_1 x_o) \end{array} \right]. \tag{39}$$

Currents in the stator frame may be referred to the rotor by inverse transforms

$$\left[\begin{array}{c} i_D \\ i_Q \end{array} \right] = e^{-\gamma_1 x_o \mathbf{J}} \left[\begin{array}{c} i_\alpha \\ i_\beta \end{array} \right] \tag{40}$$

for motors 1 and 3 ($n \in \{1, 3\}$) and

$$\left[\begin{array}{c} i_D \\ i_Q \end{array} \right] = e^{-\gamma_1 y_o \mathbf{J}} \left[\begin{array}{c} i_\alpha \\ i_\beta \end{array} \right] \tag{41}$$

[11] The use of the matrix $\mathbf{J}$ results in a very elegant, compact notation for reference-frame transformations in models of electric machines. Unfortunately, its use is not widespread. The author was introduced to the notation in a graduate course at the Massachusetts Institute of Technology where the results of Brockett [28] were applied to electric machine theory.

for motors 2 and 4 ($n \in \{2, 4\}$).

Finally, the orthogonal stator currents are resolved into a three-phase Y connection using the constant-mmf transform [29],[12]

$$\begin{bmatrix} i_A \\ i_B \\ i_C \end{bmatrix} = \begin{bmatrix} \sqrt{\frac{2}{3}} & 0 \\ -\sqrt{\frac{1}{6}} & \sqrt{\frac{1}{2}} \\ -\sqrt{\frac{1}{6}} & -\sqrt{\frac{1}{2}} \end{bmatrix} \begin{bmatrix} i_\alpha \\ i_\beta \end{bmatrix} \equiv \mathbf{C} \begin{bmatrix} i_\alpha \\ i_\beta \end{bmatrix}. \tag{42}$$

Summarizing, given force commands for each motor, three-phase currents are generated by

$$\begin{bmatrix} i_{An} \\ i_{Bn} \\ i_{Cn} \end{bmatrix} = \mathbf{C}\, e^{\gamma_1 x_o \mathbf{J}} \frac{2e^{\gamma_1 z_o}}{B_r \eta_o N_m G} \mathbf{K} \begin{bmatrix} f_{zn} \\ f_{xn} \end{bmatrix} \tag{43}$$

for $n \in \{1, 3\}$, and

$$\begin{bmatrix} i_{An} \\ i_{Bn} \\ i_{Cn} \end{bmatrix} = \mathbf{C}\, e^{\gamma_1 y_o \mathbf{J}} \frac{2e^{\gamma_1 z_o}}{B_r \eta_o N_m G} \mathbf{K} \begin{bmatrix} f_{zn} \\ f_{yn} \end{bmatrix} \tag{44}$$

for $n \in \{2, 4\}$.

[12]The transform $\mathbf{C}$ given here is power invariant. The magnitude of the total magnetomotive force in the machine is constant across the transformation. The transform used in [9] is $\sqrt{3/2}$ larger, which matches the magnitudes of the currents across the transformation. The resulting three-phase currents in [9] incorrectly provide 3/2 more power than the two-phase currents. Also, there are several sign differences in the transform in [9] which result from the unconventional spatial sequencing of the A, B, and C phases in [30], upon which the work in [9] is based.

I Measurements

A number of experimental measurements are presented in this appendix. In all cases, only motors 2 and 4 were used as the other motors on the wafer had a fault of some kind. As a result, it was necessary to constrain the platen to vertical motions only with a piece of tape, as shown in Figure 29. It was not possible to precisely align the platen over the stator. An attempt was made to align the direct axes of the platen magnet arrays at a stator electrical angle of 120 degrees, although evidence presented in Section 5 suggests that the alignment was not precise.

Vertical servoing from 20 μm to 350 μm in 10 μm steps is shown Figure 30. Noise on the response is evident, largely injected from the laser displacement sensors. On the 100 μm step, the mean of the measured vertical position is 100.05 μm, the standard deviation is 1.59 μm, and the peak-peak measurement is 12.8 μm.

A magnified view of the step from 90 μm to 100 μm is shown in Figure 31. Although somewhat obscured by noise, the rise time of the step is very similar the rise time predicted in Figure 27, namely 0.005 seconds.

The noise injected by the laser displacement sensors and the current amplifiers can be determined by measuring the unlevitated platen, which reveals the sensor noise, followed

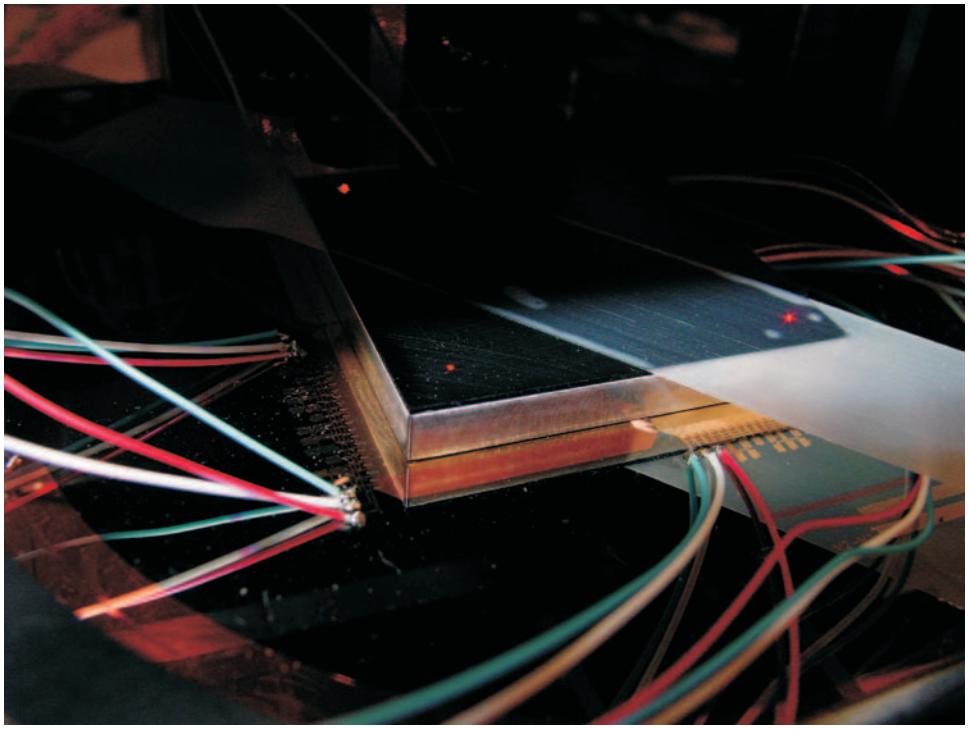

Figure 29: Platen constrained with tape to vertical motions only. Note the laser displacement sensor beams visible on the top surface of the platen.

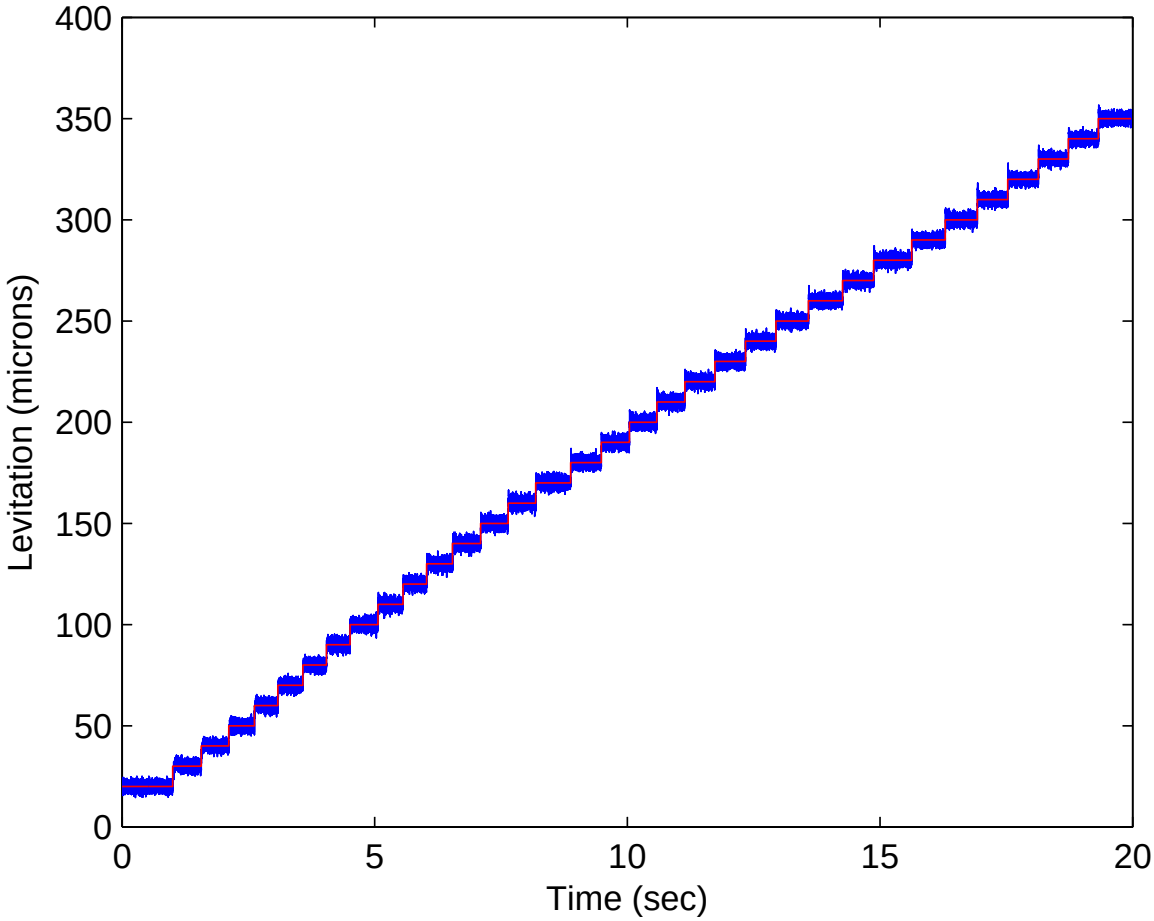

Figure 30: Measured vertical servo step response from 20 μm to 350 μm in 10 μm steps. Command shown in red. Measured levitation of the platen over motor 4 shown in blue. (Note: the steps were manually commanded and hence the widths of the steps are not uniform.)

by levitating the platen open loop in steady-state. The latter test reveals the amplifier noise after the sensor noise has been subtracted. The standard deviation of the sensor noise (specifically on the laser sensor over motor 4, although the noise on the other sensors is similar) was 1.41 μm. Curiously, the standard deviation during the open-loop test was less at 1.21 μm. Nevertheless, these results suggest that the majority of the noise observed in the closed-loop measurements is from noise injected by the laser displacement sensors.

Following constrained vertical motion tests, the tape holding the platen was removed and six degree of freedom (6-DOF) tests began using the only wafer that had more than two fully functional stators. The platen was stably levitated, although substantial jitter was observed prior to tuning the various parameters of the lateral servo loops.

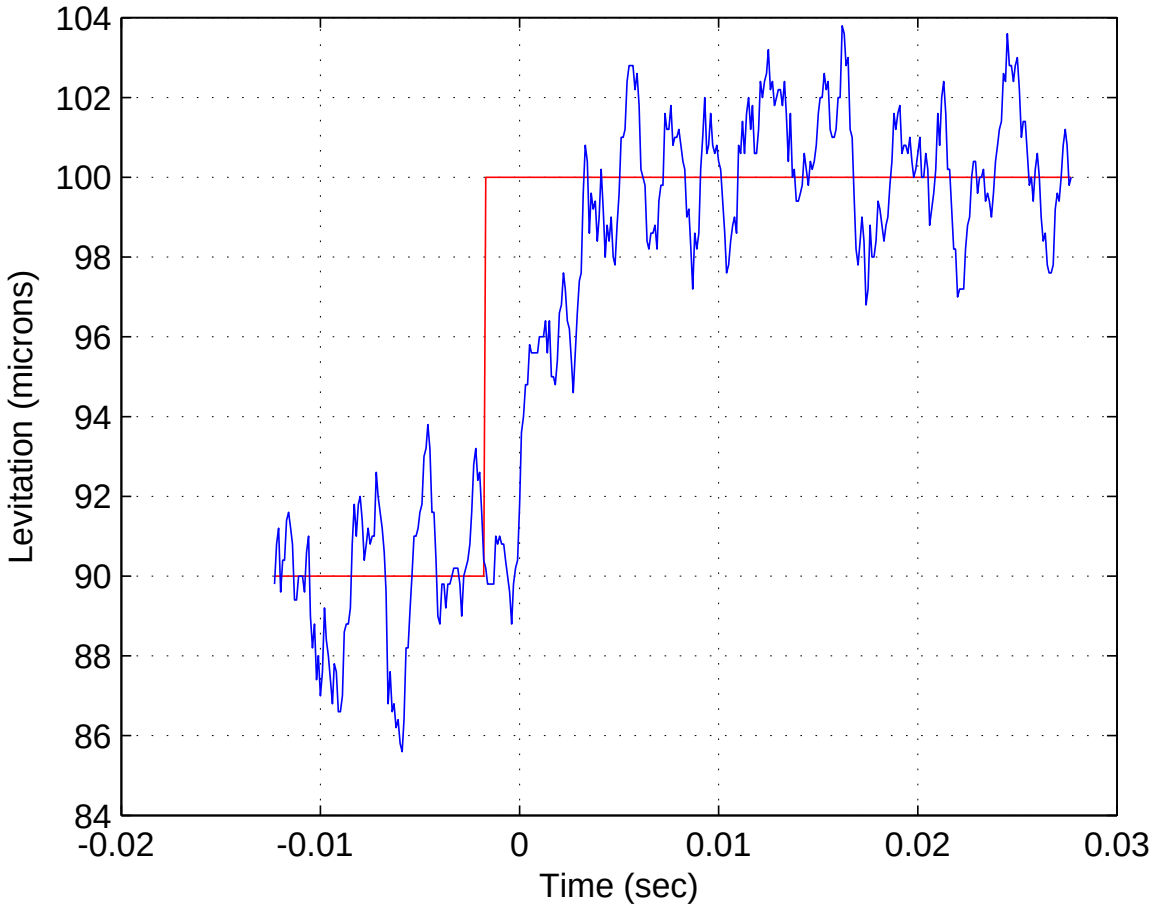

Figure 31: Measured vertical servo step response from 90 μm to 100 μm. Command shown in red. Measured levitation of the platen over motor 4 shown in blue.

Unfortunately, on one of these early 6-DOF levitation tests (though not the first one), a disturbance, most likely in the feedback position from one of the laser displacement sensors, caused the platen to bounce hard on the stator windings. Multiple sparks were observed as the armature magnets shorted the stator windings, leaving several stator phases electrically open. With no further wafers available with more than two functional stators, experiments unfortunately came to an end.

References

[1] M. Steven Rodgers et al. A new class of high force, low-voltage, compliant actuation systems. In *Solid-State Sensor and Actuator Workshop*, Hilton Head Island, South Carolina, June 4–8, 2000.

[2] Stephen F. Bart et al. Design considerations for micromachined electric actuators. *Sensors and Actuators*, 14:269–292, 1988.

[3] Herbert H. Woodson and James R. Melcher. *Electromechanical Dynamics*. John Wiley & Sons, Inc., New York, 1968.

[4] M. K. Ghantasala et al. Design and fabrication of a micro magnetic bearing. *Smart Mater. Struct.*, 9:235–240, 2000.

[5] A. R. von Hippel. *Molecular Science and Molecular Engineering*. Wiley, New York, 1959. Chs. 3 and 5.

[6] Marc Madou. *Fundamentals of Microfabrication: The Science of Miniaturization*. CRC Press, Boca Raton, FL, second edition, 2002.

[7] Patrick L. Chapman and Philip T. Krein. Smaller is better? *IEEE Ind. Appl. Mag.*, 9(1):62–67, January 2004.

[8] I. J. Busch-Vishniac. The case for magnetically driven microactuators. *Sensors and Actuators A*, 33:207–220, 1992.

[9] Won-jong Kim, David L. Trumper, and Jeffrey H. Lang. Modeling and vector control of planar magnetic levitator. *IEEE Trans. on Industry Applications*, 34(6):1254–1262, November 1998.

[10] H. Guckel et al. Micro electromagnetic actuators based on deep X-ray lithography. In *Int. Symp. on Microsystems, Intelligent Materials and Robots*, Sendai, Japan, September 27–29, 1995.

[11] Daniel J. Sadler, Sukirti Gupta, and Chong H. Ahn. Micromachined spiral inductors using UV-LIGA techniques. *IEEE Trans. on Magnetics*, 37(4):2897–2899, July 2001.

[12] Markus Ohnmacht, Volker Seidemann, and Stephanus Büttgenbach. Microcoils and microrelays—an optimized multilayer fabrication process. *Sensors and Actuators*, 83:124–129, 2000.

[13] O. Cugat et al. Deformable magnetic mirror for adaptive optics: First results. In *13th Ann. Int. Conf. on Micro Electro Mechanical Systems*, pages 485–490, Miyazaki, Japan, January 23–27, 2000.

[14] Bertrand M. Dutoit, Pierre-A. Besse, and Radivoje S. Popovic. Planar multidipolar electromagnetic actuators. *IEEE Trans. on Magnetics*, 39(2):1026–1034, March 2003.

[15] M. Nienhaus et al. Design and realization of a penny-shaped micromotor. In *Symp. on Design, Test, and Microfab. of MEMS and MOEMS*, pages 592–600, Paris, March 1999.

[16] Chunsheng Yang et al. An axial flux electromagnetic micromotor. *J. Micromech. Microeng.*, 11:113–117, 2001.

[17] V. Seidemann and S. Büttgenbach. A novel fabrication process for 3D meander shaped micro coils in SU8 dielectric and their application to linear micro motors. *Proc. SPIE Int. Soc. Opt. Eng.*, 4407:304–309, 2001.

[18] P.-A. Gilles et al. Planar double-layer coil for brushless micromotor. In *Mecatronics '01*, pages 377–382, Besançon, France, October 9–11, 2001.

[19] David L. Trumper, Mark E. Williams, and Tiep H. Nguyen. Magnet arrays for synchronous machines. In *28th IEEE Ind. Appl. Conf.*, volume 1, pages 9–18, Toronto, October 3–8, 1993.

[20] Rajen Chanchani. Interconnection technology for next generation of integrated microsystems. LDRD 26770, 2002. See ldrd.sandia.gov.

[21] Rajen Chanchani. Miniaturization of sar electronic assembly using sandia's integrated substrate technology. LDRD 52579, 2003. See ldrd.sandia.gov.

[22] Rajen Chanchani. An integrated, stacked system-on-a-chip. LDRD 52554, 2004. See ldrd.sandia.gov.

[23] P. M. Dentinger, W. M. Clift, and S. H. Goods. Removal of SU-8 photoresist for thick film application. *Microelectronic Engineering*, 61–62:993–1000, July 2002.

[24] K. Halbach. Design of permanent magnet multipole magnets with oriented rare earth cobalt material. *Nuclear Instruments and Methods*, 169:1–10, 1980.

[25] J. Ofori Tenkorang and J. H. Lang. Comparative analysis of torque production in Halbach and conventional surface-mounted permanent-magnet synchronous motors. In *30th IEEE Ind. Appl. Conf.*, volume 1, pages 657–663, Orlando, FL, October 8–12, 1995.

[26] K. Atallah and D. Howe. Application of Halbach cylinders to brushless AC servo motors. *IEEE Trans. on Magnetics*, 34(4):2060–2062, July 1998.

[27] In-Kum Kim, Robert Kratz, and David Doll. General Atomics urban maglev technology development. In *Maglev'2002*, Lausanne, Switzerland, September 3–5, 2002. Paper PP03101.

[28] Roger W. Brockett. *Finite Dimensional Linear Systems*. John Wiley & Sons, New York, 1970.

[29] N. N. Hancock. *Matrix Analysis of Electrical Machinery*. Pergamon Press, New York, second edition, 1974.

[30] David L. Trumper, Won-jong Kim, and Mark E. Williams. Design and analysis framework for linear permanent-magnet machines. *IEEE Trans. on Industry Applications*, 32(2):371–379, March 1996.

Distribution

1		Professor Won-jong Kim 221 Engineering/Physics Building Texas A&M University College Station, TX 77843-3123	
1		Professor Jeffrey H. Lang Rm. 10-176 Massachusetts Institute of Technology 77 Massachusetts Ave. Cambridge, MA 02139	
1		Professor David L. Trumper Rm. 35-016 Massachusetts Institute of Technology 77 Massachusetts Ave. Cambridge, MA 02139	
2	MS 0501	Lawrence A. Jones	2332
1	MS 0501	Arnoldo Muyshondt	2332
1	MS 0503	David W. Plummer	2330
1	MS 0507	Bruce C. Walker	2600
1	MS 0509	Michael W. Callahan	2300
1	MS 0874	Rajen Chanchani	1745
1	MS 0961	Carol L. Jones Adkins	14101
1	MS 1310	Gerard E. Sleefe,	2614
1	MS 1425	Stephen J. Martin,	1707
1	MS 0161	Patent and Licensing Office,	11500
1	MS 0323	LDRD Office,	1011
2	MS 0899	Technical Library,	9616
1	MS 9018	Central Technical Files,	8945-1